6 General-Purpose Gamma Cameras, Dedicated Gamma Cameras, and Gamma-Probes for Radioguided Surgery

Roberto Pani, Federica Guidoccio, Raffaele Scafè, Pat Zanzonico, and Giuliano Mariani

Contents

R. Pani
Department of Medical and Surgical Sciences and Biotechnologies, Sapienza University of Rome, Rome, Italy

F. Guidoccio · G. Mariani (✉)
Regional Center of Nuclear Medicine, Department of Translational Research and Advanced Technologies in Medicine and Surgery, University of Pisa, Pisa, Italy
e-mail: giuliano.mariani@med.unipi.it

R. Scafè
Department of Molecular Medicine, Sapienza University of Rome, Rome, Italy

P. Zanzonico
Memorial Hospital Research Laboratories, Department of Medical Physics, Memorial Sloan Kettering Cancer Center, New York, NY, USA

D. Volterrani et al. (eds.), *Nuclear Medicine Textbook*, https://doi.org/10.1007/978-3-319-95564-3_6

Learning Objectives

- Introduce the fundamental concepts of radionuclide imaging based on single-photon emission.
- Describe the basic components and working operations of standard gamma cameras: collimator, scintillation crystal, photomultiplier tube, position logic circuitry, signal processing, sensitivity, energy resolution, and spatial resolution.
- Describe the working principles of solid-state semiconductor detectors for dedicated gamma cameras.
- Understand the structural and operational differences between gamma cameras based on scintillation crystals and gamma cameras based on solid-state semiconductor detectors.
- Describe the main modalities of scintigraphic acquisition for planar imaging and for tomographic imaging with single-photon emission computed tomography.
- Introduce the main principles of multimodality imaging with hybrid instrumentation.
- Describe the main features of dedicated gamma cameras for cardiac imaging and for breast imaging.
- Illustrate the main principles and components of small field-of-view imaging probes.
- Illustrate the main principles and components of handheld gamma-probes for intraoperative use during radioguided surgery.

6.1 Introductory Background

Since its introduction in 1958 [1], the scintillation camera developed by Hal Anger remains the most widely used system for single photon radionuclide imaging. The success of this instrument is largely due to the simplicity of the principle of localizing the position of the γ-ray interaction with the scintillation crystal. Furthermore, continuing technological advances in growing large-volume NaI(Tl) scintillation crystals and in producing hexagonal photomultiplier tubes (PMTs) have led to the development of large size detectors, with an area sufficiently large for human studies. The intrinsic spatial resolution is optimized to image large and deep organs, where spatial resolution is dictated by the collimator properties. On the other hand, the large size and weight and the extension of a "dead" zone at the edges of the Anger camera make it difficult to position the camera for some studies, e.g., when imaging a small organ [2].

6.2 Standard General-Purpose Gamma Cameras

There are two acquisition modes for single-photon imaging: planar and tomographic [3–5]. Through planar imaging, a dual head gamma camera can acquire two projections of radiopharmaceutical distribution in the body. In clinical practice, this technique is referred to as scintigraphy. Tomography records data from multiple angles around the body, allowing visualization of radiopharmaceutical distribution in three dimensions, i.e., to display tracer distribution in various sections (slices), from a set of planar scans acquired by each detector at various rotation angles around the patient, a technique known as single-photon emission computed tomography, or SPECT.

The *gamma camera* consists of a collimator (see further below), a slab of a scintillation crystal that is optically coupled with a set of photomultiplier tubes (PMTs), and an electronic reading and data acquisition system. These components create what is usually called the "revelation head"; a gamma camera may be constituted by a single revelation head or by multiple revelation heads (most frequently two heads, more rarely three heads).

The scintillator crystal is the active part of the γ-ray detection process. When crossing the scintillator, some γ-rays pass through without interacting, while other γ-rays interact one or more times in the crystal by depositing all or part of their energy. The probability that a γ-ray of given energy E interacts with a scintillator depends on the thickness of the crystal and on the linear attenuation coefficient $\mu(E)$. This probability is given by Eq. (6.1) expressing the number $N(x)$ of photons that can cross a thickness x of the scintillator as a function of the number N_0 of incident photons:

$$N(x) = N_0 e^{-\mu(E)x} \tag{6.1}$$

The value of $\mu(E)$ depends on the atomic number Z and density ρ of the material and on the energy E of the photon. This value is usually tabulated in terms of $\mu(E)/\rho$ (mass attenuation coefficient, expressed in cm^2/g).

As scintillator material, NaI(Tl) is typically used in standard gamma cameras. Since NaI(Tl) is highly hygroscopic, the crystal is protected from external moisture by sealing within a thin aluminum housing. The inner surface of the crystal is coupled with the PMTs through a glass or quartz window (called "light guide"), while the outer surface is shielded from ambient light by an opaque cover. The mass attenuation coefficient of NaI(Tl) for 140 keV γ-rays is 0.654 cm^2/g, corresponding to a length of attenuation of about 4.2 mm.

A γ-ray can interact with the crystal scintillator through the photoelectric effect or through the Compton effect. In the photoelectric effect, the incident photon interacts with the atom as a whole; the photon is completely absorbed, causing emission of an electron with energy equal to that of the incident photon less the binding energy of the electron itself.

Instead, in a Compton interaction, the γ-ray interacts with an orbital electron. After transferring only part of its energy to the electron, the photon is diverted from its original flight direction. The residual γ-ray energy depends on its initial energy E_0 and on the deviation angle θ according to Eq. (6.2):

$$E = \frac{E_0}{1 + \frac{(1-\cos\theta)E_0}{m_e c^2}} \tag{6.2}$$

where m_e is the rest mass of the electron. The residual energy of the γ-ray varies between E_0 (value corresponding to a null angle deviation) and a minimum value E_{min} (corresponding to a deviation of 180°), as expressed by Eq. (6.3):

$$E_{min} = \frac{E_0}{1 + \frac{2E_0}{m_e c^2}} \tag{6.3}$$

In the Compton interaction, the energy transferred to the orbital electron (and therefore "measured by the scintillator") varies between 0 and a maximum value $E_{\beta max}$, called *Compton edge*, as expressed by Eq. (6.4):

$$E_{\beta\,max} = \frac{2E_0^2}{m_e c^2 + 2E_0} \tag{6.4}$$

The fundamental characteristic property of scintillating materials is to emit light in the visible (or near ultraviolet) range when a radiation γ (or X) promotes an electron from the valence band to the conduction band. In the subsequent de-energization, the electron returns to the valence band. In the case of NaI(Tl), light photons are produced for each 3 eV of energy deposited in the crystal. The light has a 415 nm wavelength. As mentioned in the previous paragraph, when a photon interacts with the material, an electron is emitted which passes from the valence band to the conduction band. While repositioning the same electron in a state of minimal energy, this goes through intermediate states that are induced in the forbidden band by suitable activating ions (or dopants). In the NaI(Tl) crystal, this role is played by thallium. When crossing these levels, a short-lived light flash (nanosecond to microseconds) is produced that can be measured by suitable photodetectors. The key point of this phenomenon lies in the fact that the amount of light produced, expressed as a whole number of photons emitted, is (almost) proportional to the energy lost by the incident photon in the interaction.

6.2.1 Photodetection

Once the scintillator has produced the light flash, this must be revealed in such a way so as to measure its total energy (which is assumed to be equal to the energy lost by the incident photon) and exact position of the interaction. The system used for this purpose was invented by Hal Anger in 1958. Although since then significant progress has been made in refining this method, the operating principle is still the same, so much so that this detector is still called the *Anger camera*. The Anger camera photodetection system consists of a set of PMTs arranged on a regular hexagonal grid and optically coupled to the scintillator crystal through an appropriate light guide. In the original Anger camera, photomultipliers were circular, while in current gamma cameras, PMTs are hexagonal, to maximize light collection (Fig. 6.1).

Each PMT provides an electrical signal that is proportional to the amount of light that has reached the PMT (a vacuum tube with a transparent input window). A material that releases electrons upon interaction with light photons is deposited on this window, which is called the photocathode. The electron emitted at the photocathode is called photoelectron (Fig. 6.2). The efficiency of this conversion (i.e., the fraction of electrons produced versus the number of photons that have reached the photocathode) is called "quantum efficiency" and is about 20–25% in modern PMTs with a typical diameter of 3″. Electrons produced during this photoconversion phenomenon are accelerated by a potential difference applied within the PMT. Here, a number of metal plates, called "dynodes," provide for multiplication (amplification) of the number of electrons. Dynodes emit multiple secondary electrons when they are hit by an electron that has been accelerated by the voltage gradient (usually

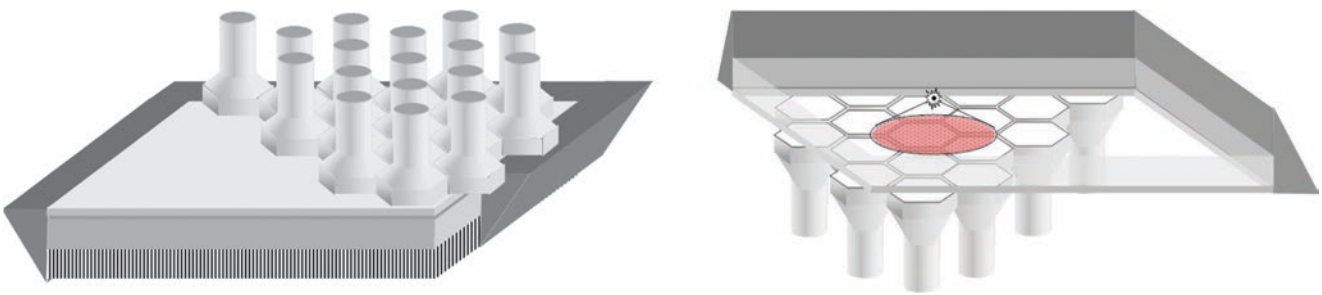

Fig. 6.1 Diagrammatic representation of the possible arrangement of hexagonal-based PMTs in a gamma camera: view from the PMT side (left) and from the scintillator side (right). Position of the collimator is also shown in the left panel. In the right panel, a scintillation event within the crystal is represented, with the resulting illumination area involving the PMT directly over the scintillation as well as the adjacent PMTs (*reproduced with permission from Volterrani D, Erba PA, Mariani G, Eds. Fondamenti di Medicina Nucleare – Tecniche e Applicazioni. Milan: Springer; 2010*)

100 V) between each dynode and the next one; the first dynode has a potential higher than that of the photocathode, and each subsequent dynode has a greater potential (or less negative) than the previous one. Thus, in the propagation of electrons between the dynodes induced by the potential difference, there are cascade multiplication effects and therefore amplification of the signal. Typically, between anode and cathode, a negative potential difference of 600–1000 V is applied, and there can be about 8–12 dynodes in a PMT. In this way, it is possible to obtain a measurable signal whose intensity is proportional to the initial number of electrons produced by the photocathode and thus to the light collected. By adding the signals from the PMTs involved in the single event, it is possible to measure an electrical signal that is proportional to the energy deposited by the incident photon.

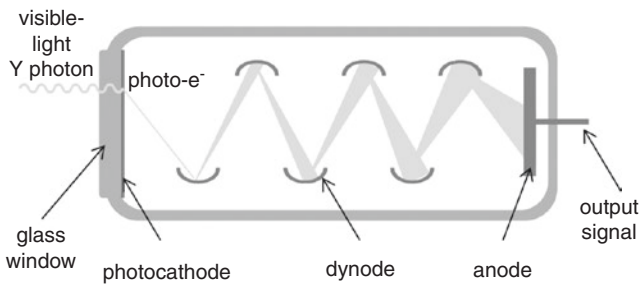

Fig. 6.2 Diagrammatic representation of the operations of a PMT (*reproduced with permission from Volterrani D, Erba PA, Mariani G, Eds. Fondamenti di Medicina Nucleare – Tecniche e Applicazioni. Milan: Springer; 2010*)

6.2.2 Signal Processing

Signals from individual PMTs are processed by an electronic system and transferred to a computer for subsequent analysis. The energy deposited by the beam of γ rays can be obtained from the sum of the electrical signals coming from the single PMTs. This information also serves as a consensus signal for the acquisition, as only signals having intensity greater than a certain threshold value are considered significant and therefore acquired (Fig. 6.3).

The coordinates *x*,*y* of the radius impact point of the γ-ray in the crystal can be determined by the spatial distribution of the recorded signals. Such definition of the position in a planar space is obtained by weighing the position of the PMT involved in each event with the intensity of the signal produced by it and calculating the mean of the values obtained. In practice, this corresponds to calculating the barycenter of the distribution of light in the crystal. In fact, the intensity of light that "illuminates" a two-dimensional array of PMTs

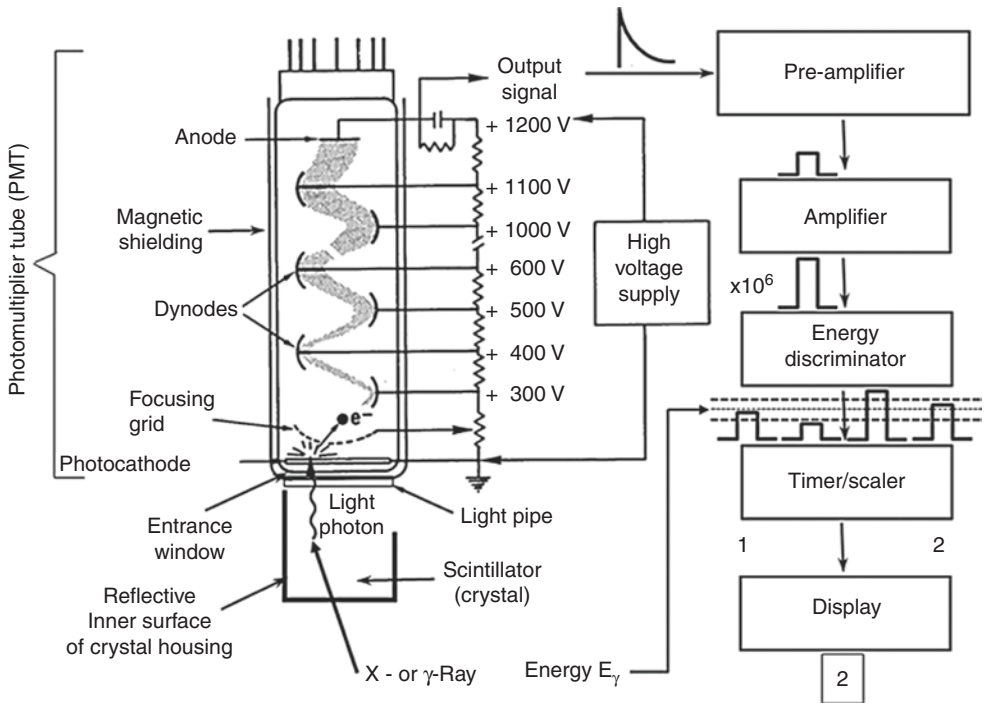

Fig. 6.3 Diagrammatic representation of a scintillation detector coupled with the PMT connected with the counting/discrimination system. Only two of the four pulses have energy levels lying between the preset pulse-height range (indicated by the two dash horizontal lines below the energy discriminators in the right part of the figure). Thus, only two photons correspond to the energies within the preset photopeak energy window and are considered for counting or for image formation. The other two photons have pulse heights (therefore energies) outside the photopeak energy window and are therefore not counted or included in image formation (*reproduced with permission from Zanzonico P. Instrumentation for positron emission imaging. In: Strauss HW, Mariani G, Volterrani D, Larson SM, Eds. Nuclear Oncology – From Pathophysiology to Clinical Applications. New York: Springer; 2017:217-50*)

varies inversely with the distance between the scintillation event within the crystal and the corresponding PMT(s). The Anger position logic circuitry is based on this inverse relationship for precisely localizing in the *x*,*y* matrix the scintillation event within the gamma camera crystal.

The sum of the signals (energy) and the center of gravity (coordinates *x*,*y*) are obtained through statistical computing techniques that use a combination of hardware, software, and the implementation of information from experimental calibration measurements. Although this technique implies a certain degree of complexity, its main advantage consists in the possibility of correcting any spatial nonlinearity when calculating the position of the γ-ray/crystal interaction as well as any local deviation from the expected value when estimating the deposited energy, based on prior appropriate calibration procedures. These are obtained through the acquisition of the γ-rays emitted by radioactive sources with regular geometry typically placed on a regular grid. Correspondence between the known positions of the sources and the measured position is stored in a correction table *(lookup table)* and used for the calibration of spatial linearity.

6.2.3 Energy Resolution

The sum of signals from PMTs is used to select only photons with energy that is included within a certain predefined range, i.e., within the energy window. The other detected photons are discarded and therefore not used for formation of the final scintigraphic image. Definition of the energy window serves to select only those photons emitted by the γ-ray source of interest and that have not undergone the Compton interaction in the subject/patient, as these would lead to a degradation of image quality. Usually the optimal energy window is selected prior to the beginning acquisition, based on the characteristics of the radioisotope used and the detection system. To this end, the characteristic parameter of a *gamma camera* is its *energy resolution*

In fact, the value provided by the PMT, intensity of the light signal due to interaction with the radius γ-rays, does not exactly match the value of the energy released in the scintillator, but there is a certain degree of fluctuation. This uncertainty on the energy of the incident γ-ray is measured by a quantity called *energy resolution*. This uncertainty stems from the fluctuation in the number of luminous photons emitted during the scintillation phenomenon, from the statistical conversion process of photons into electrons in the photocathode, and from additional fluctuation of the signal produced by the PMT during multiplication of the electrons. Energy resolution is usually expressed as $\Delta E/E$ for a given energy, i.e., as fluctuation of the energy signal, measured as the *full width at half maximum* (or FWHM) of the peak in the energy spectrum, divided by the energy value itself. In a typical clinical *gamma camera* based on the NaI(Tl) crystal and PMT system, energy resolution is approximately 10% at 140 keV. Energy resolution is a key parameter for image quality, since a better value of $\Delta E/E$ improves the ability to reject the diffused γ-rays originated in Compton interactions.

6.2.4 Gamma Cameras Based on Solid-State Detectors

Gamma cameras based on solid-state ionization utilizing semiconductor cadmium-zinc telluride (or CdZnTe) detectors are now commercially available. Although CdZnTe detectors are more expensive than NaI(Tl) crystals coupled with PMTs, as in the standard conventional Anger cameras, the solid state cameras offer several important advantages, including improved energy resolution (typically resulting in a 30% reduction of the scatter counts in the photopeak energy window) and superior intrinsic spatial resolution [6, 7]. Solid-state detectors allow direct conversion of an incident γ-photon into a certain number of electron holes that are transported to the respective electrode, thus producing a measurable electrical charge with an intensity which is proportional to the energy of the incident γ-ray.

This detection process is at variance with the detector systems based on a scintillation crystal coupled with a PMT, where the measurable electrical signal is generated through the production of secondary low-energy electrons. In particular, in the scintillation detectors, intrinsic spatial resolution is degraded by the enlargement of the light spot in the crystal, whereas, in solid-state detectors, lateral enlargement of the electron cloud is much more limited, thus resulting in better spatial resolution.

The mass density of CdZnTe is higher than that of NaI(Tl) (5.8 g/cm^3 versus 3.7 g/cm^3); however, due to higher cost and in order to ensure excellent energy resolution, CdZnTe detectors are thinner (~5 mm) than the typical 3/8″NaI(Tl) crystals (about 9.5 mm). Therefore, the intrinsic sensitivities of CdZnTe-based and NaI(Tl)-based detectors are comparable. However, the compact form factor of CdZnTe detectors permits novel detector geometries and, in turn, high-sensitivity collimation.

6.2.5 Performance

The NEMA NU-1 document "Performance Measurements of Scintillation Cameras" (2001) provides guidelines for measuring the performance of a gamma camera. This document describes the procedures to be followed for measuring (1) intrinsic spatial resolution of the detector, (2) spatial linearity, and (3) energy resolution and uniformity (differential and integral), along with the procedures for measuring performance of the combined detector-collimator system. In particular, the intrinsic spatial resolution of the detector (R_γ) is defined as the semi-FWHM of the image reconstructed from a point source. The value of R_γ depends on the characteristics of the scintillator and of the photodetector.

In general, R_γ is approximately 3–5 mm, and it depends on the thickness of the crystal, the number of PMTs per unit of surface, the positioning algorithm used, and the radius energy incident γ-rays. It should be emphasized that spatial resolution improves with increasing energy of the incident γ-rays and therefore depends on the radioisotope used.

Spatial resolution worsens with increasing thickness of the crystal, because of the greater enlargement of the light spot that reaches the PMTs. On the other hand, thickness of the crystal cannot be too small, as it directly affects the detection efficiency, as described in Eq. (6.1).

6.3 Single-Photon Emission Computed Tomography (SPECT)

The detectors described above are used to obtain projection images of radionuclide distribution within the source of interest (body of the patient), each acquisition yielding a two-dimensional representation on the *x*,*y* axes, i.e., a planar view. A SPECT gamma camera system allows acquisition of multiple planar, angular views of the source of interest yielding scintigraphic images that represent radionuclide distribution in three dimensions.

In planar emission imaging, the intensity observed in a given area of the image is a function of the amount of radioactivity present along a given propagation direction, which is selected by using an appropriate collimator (see further below). The resulting image is therefore a two-dimensional projection of the actual distribution of activity in the body, which is intrinsically three-dimensional. By changing the angle of the detector equipped with, e.g., a parallel-hole collimator with respect to the patient, it is possible to obtain an image where some details, which in the previous image were covered by other structures, become more obvious. The second image will still be planar, i.e., two-dimensional, but from a different angle. With *tomography*, the information obtained by measuring at various angles the intensity of the radiations emitted by a certain source are suitably combined, by means of a computer, to reconstruct the image of a section (or "τομος" in Greek) of the patient's body. In a tomographic section, a given area within the image has an intensity that is directly related to the local radioactivity concentration, and each structure in the section is visible because in certain angle(s) it is not covered by other structures. Therefore, the section (or *slice*) is not affected by "overlap" problems, which are typical of planar imaging.

In the case of SPECT with parallel-hole collimators, reconstruction of 3D images can be reduced to a 2D problem considering how images of individual projections planar are recorded. In fact, for each angular position radioactivity distribution is projected onto the detector that "acquires" an image that typically has a 64 × 64 or 128 × 128 pixel size. Thus, each line of the matrix records projections originating always from the same section of the source object (Fig. 6.4).

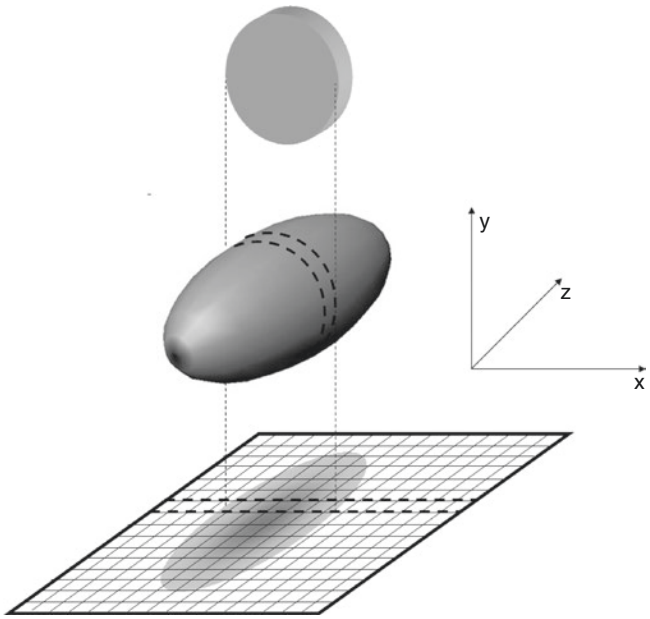

Fig. 6.4 Each row of the matrix records views/projections that always come from the same section of the source object (*reproduced with permission from Volterrani D, Erba PA, Mariani G, Eds. Fondamenti di Medicina Nucleare – Tecniche e Applicazioni. Milan: Springer; 2010*)

Data from each section of the object is therefore separated and can be reconstructed independently of each other.

Figure 6.5 summarizes the acquisition of data from a single slice. For each angular position of the detector, a histogram (profile) is obtained that shows, for each detector element, the intensity of the measured radiation. This will represent the value of the line integer for each flight loop defined by the detector element. Starting from such intensity profiles, a suitable tomographic reconstruction software yields the reconstructed 2D image of the slice itself. Combination of the various slices therefore allows reconstruction of a 3D image of the unknown distribution ($\rho(x,y,z)$) of the radiotracer within the body.

A tomographic acquisition is considered "complete" when the projections have been acquired from a number of angular positions over an arc of at least 180°. It should be noted that, after a 180° rotation, the flight directions of the γ-rays that are acquired are the same as the acquisition at 0°, while what changes is the direction of propagation.

A SPECT tomograph is usually made up of one or more gamma camera detectors (usually two, sometimes three detectors), each coupled with its own collimator and capable of rotating around the patient's body. The system is connected to a computer that must control both data acquisition and mechanical rotation of the detectors. There are two rotation modes commonly used in SPECT, the so-called "continuous rotation" mode and the "step-and-shoot" mode. In the continuous rotation mode, the detectors are rotated at constant speed around the patient, and the data so acquired is then grouped into a finite number (typically 64 or 128) of angular values (or projections).

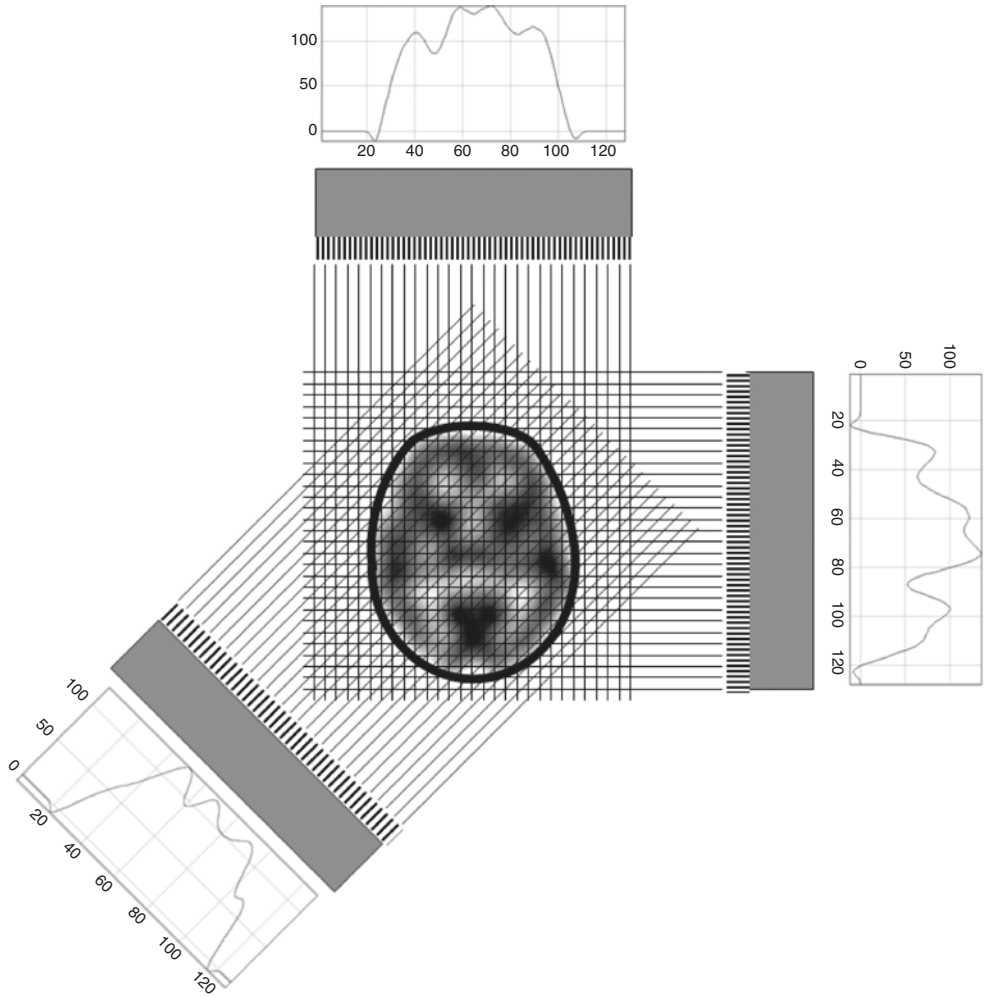

Fig. 6.5 Diagrammatic representation of the matrix data acquired simultaneously with a three-head gamma camera for SPECT (*reproduced with permission from Volterrani D, Erba PA, Mariani G, Eds. Fondamenti di Medicina Nucleare – Tecniche e Applicazioni. Milan: Springer; 2010*)

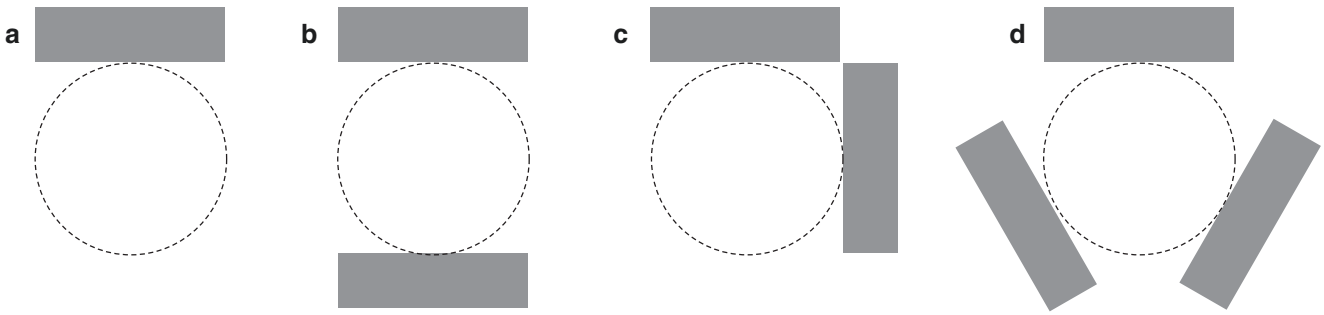

Fig. 6.6 Possible configurations of the revelation gamma camera heads for acquisition of SPECT data. (**a**) single head; (**b**) two opposing heads; (**c**) two heads at a 90° angle one to another; (**d**) triple head (*reproduced with permission from Volterrani D, Erba PA, Mariani G, Eds. Fondamenti di Medicina Nucleare – Tecniche e Applicazioni. Milan: Springer; 2010*)

In the step-and-shoot mode, the rotational motion stops at various angular positions (corresponding to the angles for which you want to acquire a projection) and remains stationary until the data have not been acquired, after which it moves on to a next angle; 3° or 6° angular steps are usually employed.

SPECT systems differ from one another according to the number of gamma camera revelation heads, which typically can be one to three. The higher the number of detectors used, the greater the overall sensitivity of the instrument, which increases linearly with the number of detectors used. In particular, assuming a certain number of total events to be acquired during tomography, a three-head gamma camera will complete acquisition in exactly one-third the time required by acquisition with a single-head gamma camera.

Figure 6.6 shows the most common configurations for SPECT detection heads: (a) single head, (b) two opposing heads, (c) two heads at 90°, and (d) triple head. Usually, two-head gamma cameras can vary the position of the two heads

in configurations (b) or (c). This is useful when using SPECT as a planar imaging system to simultaneously obtain anterior and posterior (b) or anterior and lateral (c) views. In case of the (a) and (b) configurations, a complete tomographic acquisition can only be obtained by rotating the detectors by 180°, while with the (c) configuration, a 90° rotation is sufficient, and with the (d) configuration, a 60° rotation is sufficient. In order to achieve better sampling of the entire field of view, it is preferable to acquire the same direction of flight from γ-rays along both sides, so as to mediate the effects of attenuation that γ-rays undergo while crossing the body (see further below). For full coverage of the entire field of view, the detector(s) must rotate by 360° (configuration a), 180° (configurations b and c), or 120° (configuration d).

6.4 Collimators

The most important issue regarding intrinsic spatial resolution of SPECT is the need for reaching an optimal trade-off between spatial resolution and sensitivity that both depend on the characteristics of the collimator(s) used. Therefore, optimization and choice of the collimator(s), also in relation to the specific clinical application, are the crucial factors affecting the whole image quality in single-photon emission imaging. Collimators are usually classified according to construction material, geometry, and shape and size of holes.

6.4.1 Materials

Ideally, a collimator works like a binary filter. When a γ-ray photon hits the collimator, it can reach the detector only if its flight direction respects the geometric conditions defined by the collimator holes. This "selection" is based on the absorption of the γ-rays whose flight directions do not meet the same conditions but also on secondary events taking place upon the γ-ray/collimator interaction. In fact, some γ-rays that propagate in a direction not parallel to the collimator's holes will pass through the collimator material without interacting (this phenomenon is called "penetration"), while others may undergo Compton interactions; in the latter instance, some Compton-diverted photons reach the scintillator in spots that do not exactly mirror the original flight direction. In both instances (penetration and Compton scattering), unintended photons can contribute to formation of the final image, thus degrading its quality.

To reduce these phenomena, collimators are usually made of materials with high-absorption power for γ-rays, especially materials with a probability of photoelectric interaction greater than the probability of Compton scatter. In practice, the materials chosen have a high atomic number, Z, and high density, ρ. The most commonly used materials are lead alloys (Z = 82, ρ = 11.3 g/cm^3), followed by tungsten alloys (Z = 71, ρ = 19.1 g/cm^3) or gold (Z = 79, ρ = 19.3 g/cm^3). However, tungsten and especially gold alloys are less frequently used due to the difficulty of tungsten processing and the high cost of gold.

6.4.2 Geometry

Collimator geometry defines the geometric condition of "acceptance" for incident photons on the gamma camera head. Various types of collimators are used, including parallel-hole collimators, the converging-hole or diverging-hole collimators, and pinhole collimators. Collimators with specific, dedicated applications include the slanted-hole collimator.

6.4.2.1 Parallel-Hole Collimators

A parallel-hole collimator consists of a block of γ-ray-absorbing material where parallel holes are perforated, perpendicular to the detector. This is the geometry most commonly used for gamma camera imaging, as it provides wide-field views and yields a real-size projection of radioactivity distribution within the patient's body.

Ideally, a parallel-hole collimator allows only the γ-rays that travel in an orthogonal direction to the detector. In practice, due to finite size of the section of the holes, the collimator accepts photons with an angle of incidence included within a certain *range* of values. Therefore, increasing the diameter of the holes, as well as reducing their length, worsens spatial resolution. Each hole of a parallel-hole collimator defines a cone whose angular opening is given by Eq. (6.5):

$$\vartheta_{\mathrm{Tot}} = \frac{D}{L} \tag{6.5}$$

where D and L are the diameter (considered in this case circular) and length of the holes, respectively. Therefore, the geometric spatial resolution R_c (estimated as *FWHM* of the *point spread function* or *PSF*) is given by Eq. (6.6):

$$R_c = D\frac{(d+L)}{L} \tag{6.6}$$

As a consequence, increasing the distance of a source object from the collimator by increasing the diameter of the underlying cone worsens spatial resolution, which instead improves by keeping the source object closer to the collimator. Optimal positioning of the parallel-hole collimator holes is the position that minimizes the distance of the source object from the collimator surface.

If the detector behind the collimator has a spatial resolution, R_r, the system will therefore have a FWHM of spatial resolution given by Eq. (6.7):

$$R_s = \sqrt{R_c^2 + R_r^2} = \sqrt{\left(D + d\frac{D}{L}\right)^2 + R_r^2} \tag{6.7}$$

On the other hand, geometric efficiency of a parallel-hole collimator, ϵ_c, measured as the fraction of photons that are

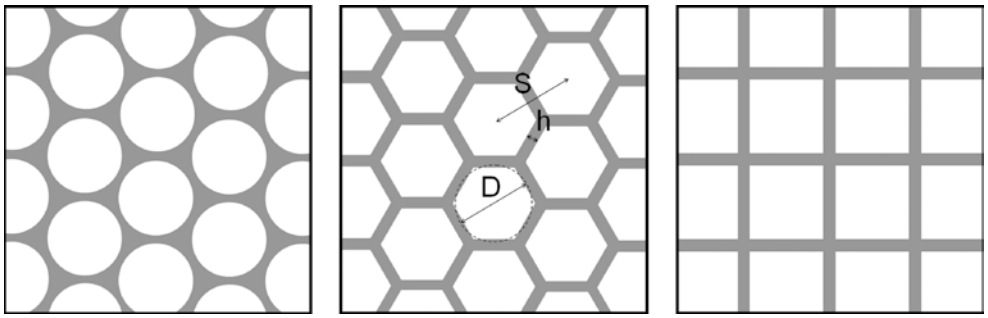

Fig. 6.7 Most common shapes of the holes in parallel-hole collimators: round holes (left), hexagonal holes (middle), square holes (right). *D* = diameter of each hole; *S* = space between two adjacent holes; *h* = thickness of the septa (*reproduced with permission from Volterrani D, Erba PA, Mariani G, Eds. Fondamenti di Medicina Nucleare – Tecniche e Applicazioni. Milan: Springer; 2010*)

accepted by the collimator versus the total number of photons emitted by the source, is given by Eq. (6.8):

$$\epsilon_c = K^2 \left(\frac{D}{L}\right)^2 \frac{D^2}{(D+h)^2} \tag{6.8}$$

where h is the minimum thickness of the septum between the holes and K is a factor that depends on the geometry of the holes.

It is important to note that the efficiency of a parallel-hole collimator does not depend on the distance between the source object and the collimator. In fact, ignoring the attenuation effects on the emitted γ-rays, all areas within a certain field of view will be measured with the same efficiency. Typical orders of magnitude of the efficiency values of parallel hole collimators may vary between 10^{-4} and 10^{-6}.

The holes in the collimator are usually made in three shapes: hexagonal holes in a hexagonal grid, circular holes on a hexagonal grid, and square holes in a square grid (Fig. 6.7). Since the collimator structure is periodic, the collimator's characteristics are uniquely determined by thickness of the holes but also by their shape, size, and separation. Size of the hole is usually indicated by the diameter, *D*. While in the case of circular holes, the meaning of *D* is immediate, in the case of hexagonal or square holes, *D* expresses the value of the diameter of the circle having the same area as the hole that is being considered.

As for separation between the holes, the value *S* indicates the distance between the centers of two adjacent holes. In many cases, however, separation between the holes is expressed in terms of thickness of the septum (*h*), as this parameter provides more direct information on the collimator ability to stop the photons traveling in directions that are oblique with respect to the axis of the holes. In the case of hexagonal and square holes, *h* simply indicates the thickness of the material that separates two adjacent holes, while in the case of circular holes, it indicates the minimum thickness.

For added convenience, parallel-hole collimators for clinical applications are not classified according to shape/size of the holes and thickness of the septa, but simply according to their spatial resolution and relative efficiency and their *range* of application energies. This simplifies their choice depending on the use required for a specific diagnostic application, regardless of the different parameters that a manufacturer can choose to achieve the same or similar characteristics. This classification refers to the *range* of γ-rays energy (therefore of radionuclides) for which the collimator may be used and the best trade-off between spatial resolution and sensitivity. The most common types of parallel-hole collimators are classified as:

- Low-energy, high-resolution (LEHR) collimators are used with radionuclides that emit γ-rays of low energy, in order to achieve high spatial resolution at the expense of sensitivity.
- Low-energy, all-/general-purpose (LEAP or LEGP) collimators are used with radionuclides that emit γ-rays of low energy, in order to achieve an optimal trade-off between spatial resolution and efficiency.
- Medium-energy, all-/general-purpose (MEAP or MEGP) collimators are used with radionuclides that emit γ-rays of intermediate energy, in order to achieve optimal trade-off between spatial resolution and efficiency.
- High-energy, all-/general- purpose (HEAP or HEGP) collimators are used with radionuclides that emit γ-rays of high energy, in order to achieve optimal trade-off between spatial resolution and efficiency.

Collimators classified as LE (low energy) are usually recommended for ^{57}Co (122 keV), ^{123}I (159 keV), ^{99m}Tc (140 keV), and ^{201}Tl (69–81 keV); ME collimators are used for ^{67}Ga (93, 184, and 296 keV) and ^{111}In (172 and 247 keV); HE collimators are commonly used for ^{131}I (284 and 364 keV).

6.4.2.2 Converging- or Diverging-Hole Collimators

For some particular applications, it may be useful to use collimators that have holes that, instead of being mutually parallel, are plotted along convergent or divergent directions. Converging-hole collimators magnify the image of the source object on the detector; they can therefore be used only with source objects that have size smaller than the detector. Thanks

to their particular geometry, these collimators are inherently more efficient than parallel-hole collimators. Because of these properties (magnification of the image and increased counting efficiency), these collimators may be used to image relatively small source objects with increased sensitivity or with better spatial resolution—depending on the design of the collimator.

Instead, diverging-hole collimators are used in those cases where one wishes to image a source object larger than the detector. For either converging- or diverging-hole collimators, the main drawback consists in providing distorted images of the distribution of activity in the field of view, since the magnification factor depends on the distance of the object source from the collimator. This fact is important especially for planar imaging; a SPECT acquisition can be corrected through accurate modeling of the collimator to be applied in the algorithm of image reconstruction.

6.4.2.3 Pinhole Collimators

Especially for high-resolution imaging, *pinhole* collimators may be used. These consist of a single hole with a double cone shape (Fig. 6.8). The rationale of image acquisition with such collimators is similar to that of the darkroom used in photography. In fact, these collimators yield on the detector an image of the source object that is inverted and magnified (or downsized, depending on the object distance of the source object from the collimator) with respect to the actual size of the object. Although use of these collimators yields high spatial resolution (e.g., by exploiting to the maximum magnification and using a pinhole with a very small hole), counting efficiency drops very quickly with increasing distance between the hole and the source object.

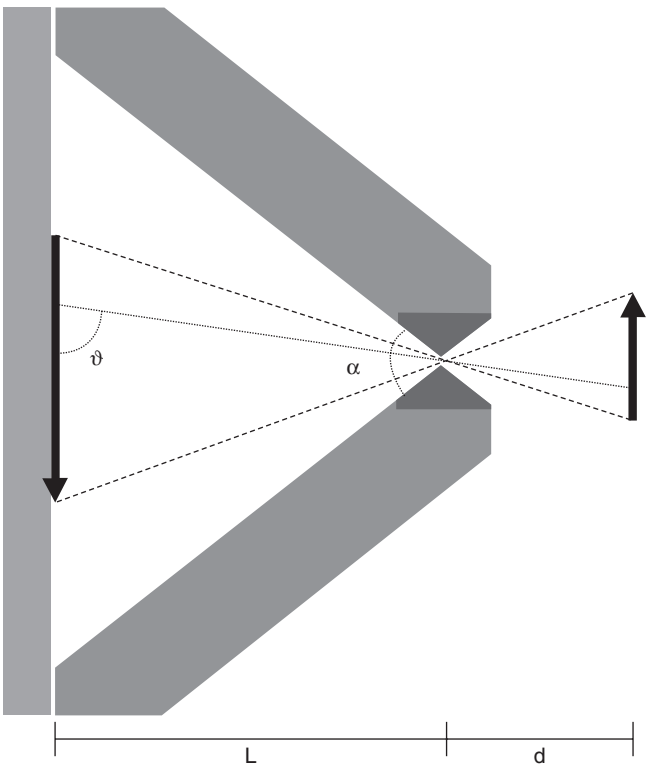

Fig. 6.8 Diagrammatic representation of a pinhole collimator (see text) (*reproduced with permission from Volterrani D, Erba PA, Mariani G, Eds. Fondamenti di Medicina Nucleare – Tecniche e Applicazioni. Milan: Springer; 2010*)

In fact, geometric efficiency is given by the fraction of solid angle subtended from the hole from a certain point of the field of view. The geometric efficiency of a pinhole collimator ε_p is given by Eq. (6.9):

$$\epsilon_p = \left(\frac{D}{4d}\right)^2 \sin^3 \vartheta \tag{6.9}$$

where D is diameter of the hole, d is the distance between the object source and the hole, and ϑ is the angle that the incident photon forms with the plane of the detector, as shown in Fig. 6.8. Therefore, efficiency is inversely related to the square of the distance (αd^{-2}), thus decreasing as the distance d increases, as well as with increasing from the axis of the pinhole (as a proportion of $\sin^3\vartheta$). Figure 6.9a plots the performance efficiency of a *pinhole* collimator as a function of the distance d of the object from the hole. It should be noted that, unlike a parallel-hole collimator, efficiency varies with d and the *pinhole* collimator is more efficient only at small distances, whereas it drops dramatically for large values of d.

Besides efficiency, distance d from the collimator affects also the size of the field of view. In fact, the field of view of a pinhole collimator is defined as the cone projected from the detector through the pinhole. In particular, the field of view increases in a linear fashion with distance d, but on the other hand efficiency is greater for small values of d, where the field of view is minimal (Fig. 6.9b).

For a pinhole collimator, the FWHM of spatial resolution, R_p, is given by Eq. (6.10):

$$R_p = D_e \frac{(d+L)}{L} \tag{6.10}$$

Therefore, for values of d much smaller than L, spatial resolution is practically given by the value of D_e, which is the effective diameter of the hole. This value is greater than the nominal diameter of the hole, because the radiation impinging in the *pinhole* can penetrate into the material in the vicinity of the edge of the hole, where thickness is a minimum. D_e depends not only on the geometric diameter D but also on the linear attenuation coefficient of the material, μE, constituting the collimator (and hence the energy E of the incident radiation), and on its defined aperture angle α. The value of D_e can be estimated using Eq. (6.11):

$$D_e = \sqrt{d\left(d + \frac{2}{\mu}\tan\left(\frac{\alpha}{2}\right)\right)} \tag{6.11}$$

Overall, the FWHM value for spatial resolution of a system equipped with a pinhole collimator with spatial

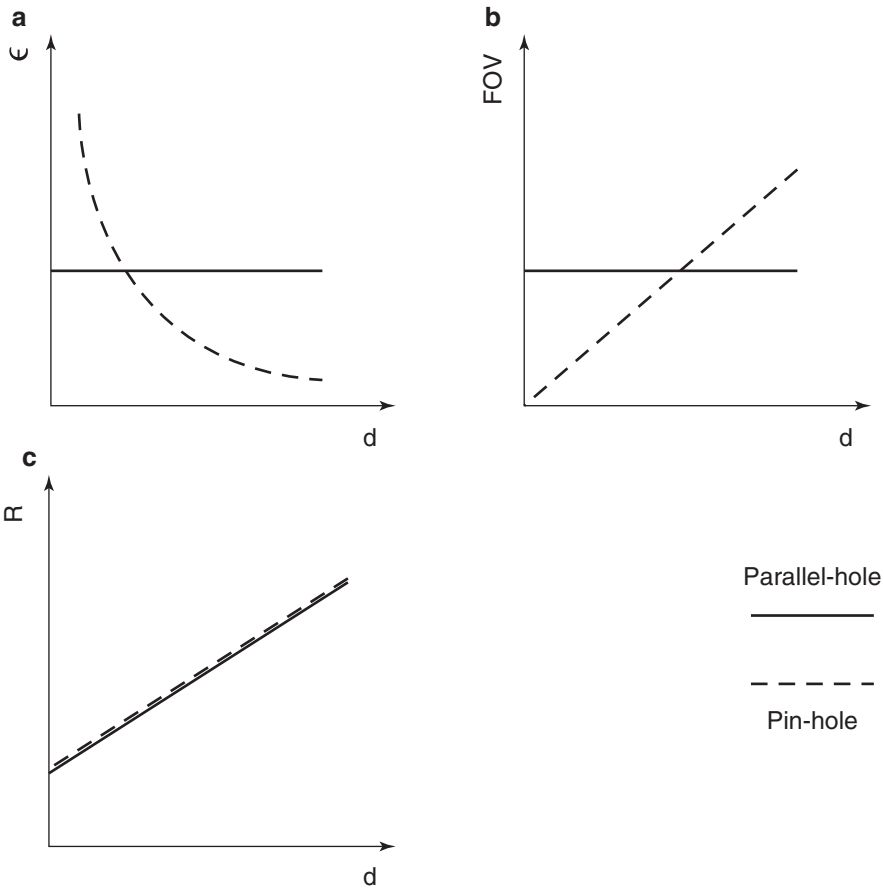

Fig. 6.9 Comparison of performances between a parallel-hole collimator (gray continuous line) and a pinhole collimator (dash black line) with respect to counting (**a**), size of the field of view (**b**), and spatial resolution (**c**) as a function of the distance "*d*" of the source object from the collimator (*reproduced with permission from Volterrani D, Erba PA, Mariani G, Eds. Fondamenti di Medicina Nucleare – Tecniche e Applicazioni. Milan: Springer; 2010*)

resolution R_p and coupled with a detection system for γ-rays with intrinsic spatial resolution R_r is given by Eq. (6.12):

$$R_s = \sqrt{R_p^2 + \left(R_r \frac{d}{L}\right)^2} = \sqrt{\left(D_e \frac{(d+L)}{L}\right)^2 + \left(R_r \frac{d}{L}\right)^2} \quad (6.12)$$

Figure 6.9c compares the intrinsic spatial resolution of a pinhole collimator with a parallel-hole collimator. The pinhole collimator has better resolution for small values of *d*, where the efficiency is at a maximum but the field of view is minimal.

For this reason, pinhole collimators are often used for high-resolution imaging of small source objects, in particular for preclinical imaging of small animals. In fact, by exploiting the magnification effect, high-resolution images of small objects (small FOV) compared to the size of the detector can be obtained, while maintaining the sensitivity that would be obtained with parallel-hole collimators. Further increased magnification can be achieved with spatial resolutions of the order of a few hundred micrometers, even with clinical gamma cameras. By using more holes (*multi pinhole* collimator), it is possible to obtain wider fields of view and at the same time to increase the overall sensitivity of the instrument. By reducing the magnification, it is thus possible to obtain high-resolution images of fields of view sufficient to display "total body" of small rodents.

Pinhole collimators are usually made of lead or tungsten. However, in order to limit the value of D_e, use of high atomic number materials, such as gold or platinum, is preferred. In order to minimize costs, it is sufficient to use such precious metals to make only the central part of the pinhole collimator that contains the hole—called "insert."

The pinhole collimator is suitable for a wide range of γ-ray energies, ranging from 20–30 keV (^{125}I) to single photon imaging of positron annihilation photons (511 keV).

6.5 Multimodality Imaging: SPECT/CT

The γ-rays emitted from the body undergo variable attenuation while traveling from the point of origin to the revelation head of the gamma camera. Attenuation is indeed a crucial factor in diagnostic imaging with standard gamma cameras, as γ-rays are attenuated according to the exponential law expressed by Eq. (6.1). For example, energy of the γ-rays emitted by ^{99m}Tc, the most widely used radionuclide for single-photon emission imaging, is 140 keV. The linear attenuation coefficient in the water (μH_2O) for photons with this energy is approximately 1.53×10^{-1} cm^{-1} corresponding to a half-thickness ($\lambda_{½}$, i.e., the thickness that halves the number of emerging photons compared to the original number of photons) of approximately 4.5 cm (note that $\lambda_{½} = \ln 2/\mu$).

It is therefore obvious that, especially in the case of SPECT acquisitions, the effect of attenuation is not negligible if one wants to quantitate absolute radioactivity concentrations within certain volumes of interest. For example, while crossing the human body (approximately 40 cm in diameter), 140 keV γ-rays would be attenuated by a factor of about 450. Considering attenuation, the integral equation along a certain line corresponds to Eq. (6.13):

$$N_\gamma(x,z) = \int_L \rho(x,z,y)\, e^{-\int_{L'} \mu(x,z,y',E)\,dy'}\, dy \qquad (6.13)$$

where L is the line along which the activity $\rho(x,y,z)$ is measured (integrated) and L' is the actually traversed line by a photon emitted from point $P(x,y,z)$ and directed along the line L, while $\mu(x,y,z)$ is the local value of the linear attenuation coefficient for photons with given energy photons E (Fig. 6.10).

Clearly, in order to obtain true distribution of the activity at various depths within the body or to be able to provide a quantitative estimate, it is necessary to know a priori the distribution of the linear attenuation coefficients for the given energy.

In the stand-alone SPECT instrumentation, this measurement was based on acquisitions "in transmission" where a radioactive source (linear or planar) was used to obtain some sort of a tomographic image (similar to CT) that would provide information on the distribution of attenuation coefficients (the so-called μmap); alternatively, theoretical attenuation coefficients based on phantom data mimicking composition of the body were utilized. In modern SPECT gamma cameras correction for attenuation is obtained by coupling the SPECT system with a CT scanner, through the use of a multimodal imaging instrument called SPECT/CT. In this way, the μmap to correct for attenuation can be obtained directly from the CT data, by suitably rescaling the values of $\mu(E)$ obtained with the X-rays energy of CT to the energy values of the γ-rays used for SPECT.

As an added value, the SPECT/CT systems provide, together with the functional images of SPECT, the possibility to overlap each reconstructed γ-ray emission slice onto the corresponding anatomical structures depicted by the X-ray transmission scan. This property can greatly assist diagnostic interpretation, by providing complementary morphological information that, considering the relatively low spatial resolution and inherently functional nature of the SPECT image, were not present in the emission image alone.

It should, however, be emphasized that, unlike PET/CT, the CT component integrated in the SPECT/CT systems usually has physical performances inferior to those of a true clinical CT (i.e., it yields a lower diagnostic value), because the system is optimized for complementary use of CT with SPECT. These systems are therefore usually characterized by poorer spatial resolution than clinical CT scanners; furthermore, the CT component of the scan is optimized so as to confer to the patient a radiation dose lower than that of clinical CT, therefore not significantly increasing the overall radiation dose to the patient over the radiation burden caused by radiopharmaceutical administration for the SPECT scan per se.

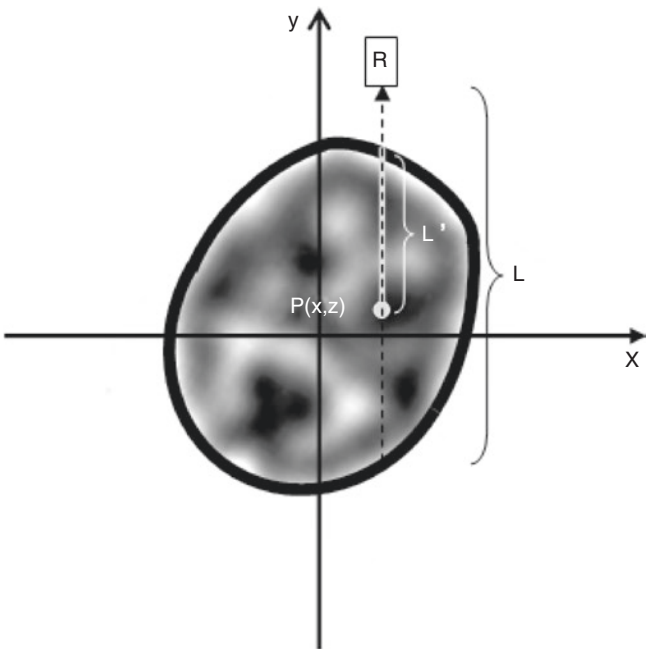

Fig. 6.10 Diagrammatic representation of the acquisition process of γ-ray emission data along a certain projection line in the presence of attenuation. The emission point $P(x,z)$ contributes to the integral of counts along line L, subject to an attenuation factor due to crossing of the emitted photons along line L' (*reproduced with permission from Volterrani D, Erba PA, Mariani G, Eds. Fondamenti di Medicina Nucleare – Tecniche e Applicazioni. Milan: Springer; 2010*)

Key Learning Points

- The two fundamental modes of single-photon imaging are planar and tomographic.
- The revelation head of a standard gamma camera consists of a collimator and of a scintillation crystal optically coupled with a set of photomultiplier tubes.
- Gamma-rays interact with the crystal by depositing all or part of their energy, which is transformed into release of a scintillation photon, through either the photoelectric effect and through the Compton effect.
- The light flash produced by interaction of γ-rays in the scintillation crystal is converted into an electrical signal by a photodetection system composed of a set of photomultiplier tubes.

- Signals from individual photomultipliers are processed by an electronic system and transferred to a computer for subsequent analysis allowing definition of the *x*,*y* coordinates of the point of the scintillation crystal where interaction of the incident γ-ray with the crystal matrix takes place.
- The fundamental parameters that characterize the imaging performance of a standard gamma camera are spatial resolution and energy resolution.
- Gamma cameras based on solid-state ionization use semiconductor detectors that achieve better energy resolution and better intrinsic spatial resolution than scintillation detectors.
- The parameters that define the imaging performance of gamma cameras include spatial resolution, spatial linearity, energy resolution, and uniformity.
- SPECT images provide information on radionuclide distribution within the body based on acquisition of multiple planar views at variable angles around the patient's body.
- SPECT images can be produced using either single-head, two-head, or triple-head gamma cameras.
- Collimators are made of high-absorption power for γ-rays and are designed to select γ-rays with directions defined by certain geometric conditions.
- According to geometry of the holes, collimators are defined as parallel-hole collimators, converging-hole or diverging-hole collimators, and pinhole collimators.
- Collimators with specific, dedicated applications include the slanted-hole collimator.
- The most common types of parallel-hole collimators include low-energy, high-resolution collimators; low-energy, all-/general-purpose collimators; medium-energy, all-/general-purpose collimators; and high-energy, all-/general- purpose collimators.
- Hybrid SPECT/CT allow multimodality imaging that has the advantages of providing morphologic anatomic correlates for the sites of radiopharmaceutical uptake and of allowing correction for actual attenuation of γ-rays based on the transmission data obtained by the X-ray beam.

6.6 Dedicated Gamma Cameras

Conventional Anger cameras using NaI(Tl) scintillation crystals coupled to a bulky array of PMTs are precluded from use in all the applications where light weight, small size, easy handling, and close positioning are required. Furthermore, the standard Anger camera suffers from intrinsic poor spatial and energy resolution.

Interest has recently emerged in developing compact gamma cameras with improved imaging performances. This has led to design new gamma cameras mainly falling into three categories: (1) semiconductor detectors, such as cadmium telluride (CdTe) or cadmium-zinc telluride (CdZnTe), in which the γ-rays interact directly with a position-sensitive solid-state detector; (2) scintillation crystals coupled to an array of solid-state photodetectors (photodiodes or silicon-avalanche photodiodes); or (3) scintillation crystals coupled with a position-sensitive PMT (PSPMT).

By using scintillation crystal arrays coupled with PSPMT, compact gamma cameras with high spatial resolution and relatively low cost can be assembled. Finally, smaller devices, based on the same principles, but scaled down to intraoperative dimensions, have been successfully developed as imaging probes for use during radioguided surgery [2]; in fact, conventional gamma cameras (even single-head—but especially multiple-head gamma cameras) cannot be housed in the surgical suite.

The above considerations have started the idea of using a different specific device for each diagnostic application, instead of only one general-purpose instrument—not unlike the variety of diagnostic equipment of a modern radiology division [8].

Intrinsic spatial resolution of an imaging system such as the Anger camera, which is based on a single large planar detector, is worse than that of collimator for a short source-to-collimator-face distance. Furthermore, the coarse image digitization (usually 3.2 mm) places additional limits to the resolution and contrast values that can be achieved.

On the other hand, advancing knowledge in biology at the molecular level and the development of new radiopharmaceuticals have generated demands for imaging devices as additional or alternative tools to the Anger camera, in order to optimize radionuclide imaging for specific biological and clinical requirements. Technological advances in the fields of photodetectors and of scintillators, as well as in electronics, encouraged the development of dedicated imagers for new diagnostic techniques in quite all the fields of functional radionuclide imaging. The main feature of such new detectors is a compact design that allows optimized anatomical fitting. Furthermore, such detectors are suitable for combined use with other diagnostic imaging modalities, so as to provide co-registered and fused images where intrinsic spatial resolution of the γ-ray emission image becomes comparable with the values achieved with radiologic imaging (around 0.4 mm).

6.7 Basic Components of Dedicated Gamma Cameras and Small FOV Imaging Probes

6.7.1 Scintillation Materials

The basic components of general-purpose gamma cameras, dedicated gamma cameras, and probes for radioguided surgery intrinsically include a detector system to convert into an electrical pulse the charge collected in the interaction between the γ-ray emitted by the source of interest and the exploring probe. After preliminary selection of the incoming γ-rays through suitable collimation, the first material that interacts with γ-rays and initiates the whole detection process is either a scintillation crystal (usually inorganic) or a semiconductor material.

As mentioned above, NaI(Tl) is the first in a long series of scintillation materials suitable for standard gamma cameras; on the other hand, its use is not suitable for small-area pixelated cameras because of drawbacks due to temperature-depending cracking effect which hampers the light output from small-sized crystals. Among others, thallium-doped cesium iodide [CsI(Tl)], bismuth germanate (BGO), and cerium-activated yttrium aluminum perovskite [YAP(Ce)] have been introduced into clinical use, as they do not suffer from the cracking effect.

Semiconductor detectors of clinical interest include cadmium telluride (CdTe) and cadmium-zinc telluride (CdZnTe), currently used in gamma-probes for radioguided surgery and in dedicated gamma cameras, e.g., for cardiac imaging or for small field-of-view (FOV) imaging.

6.7.1.1 NaI(Tl)

Robert Hofstadter (Nobel Laureate of 1961) described in 1948 the luminescence from a small NaI(Tl) crystal under γ-ray irradiation; this observation started up a long and bright career of the scintillator which continues up until today [9]. In fact, this discovery constituted the milestone marking the beginning of new horizons for nuclear medicine, leading to the development in 1956, only 8 years later, of the Anger gamma camera [1].

6.7.1.2 CsI(Tl)

A couple of years after describing the scintillation properties of NaI(Tl) crystals, Robert Hofstadter reported similar observations with other luminescent materials, such as CsI(Tl), which has subsequently been used particularly for pixelated imaging probes or for small FOV gamma cameras but also as a detector in nuclear physics [10].

6.7.1.3 BGO

The luminescence properties of BGO under X-ray irradiation were first described in 1973 [11], with an emphasis of its higher stopping power for γ-rays than the NaI(Tl) crystals. Nevertheless, BGO crystals have lower light output and higher refractive index at emission wavelength than NaI(Tl) crystals, thus being less suitable for scintillation light readout. After having been originally proposed for applications such as image intensifier screens, BGO-based detectors have actually become a standard for positron emission tomography (PET).

6.7.1.4 YAP(Ce)

Although spectral data on YAP(Ce) were also published in 1973, initial studies were really geared to laser applications. It was only in 1991 that the first results on the use of YAP(Ce) for the detection of ionizing radiation were published [12]. The light efficiency of YAP(Ce) crystals (that are not hygroscopic) is about 40% the efficiency of NaI(Tl) crystals. Because of the yttrium atomic number ($Z = 39$) and the relatively high density (5.37 g/cm^3), YAP(Ce) has a good γ-ray absorption.

6.7.2 Other γ-Ray Detectors

Solid-state detectors, also known as semiconductor ionization detectors, utilize CdZnTe as the material that interacts with the incoming γ-rays to produce an electrical pulse. Although these detectors are more expensive than the most common NaI(Tl) scintillation crystal used in standard gamma cameras, they offer several important advantages. In particular, their density is higher than that of NaI(Tl) (5.8 g/cm^3 versus 3.7 g/cm^3), thus resulting in greater stopping power for the incoming γ-rays. Furthermore, they are characterized by improved energy resolution (thus reducing by 30% the scatter counts in the selected energy window) and superior intrinsic spatial resolution. However, in order to keep the overall cost of such detectors comparable to the cost of NaI(Tl)-based detectors, CdZnTe detectors are usually kept thinner (around 5 mm) than conventional NaI(Tl) crystals (around 9–10 mm); therefore, with these parameters, the intrinsic sensitivities of the two types of detectors are comparable.

6.7.3 Arrays of Scintillation Detectors

Clusters of individual NaI(Tl) scintillation detectors arranged around a target for detecting the γ-rays produced by (α,n) reactions under irradiation of a target by a beam of α particles have been utilized in nuclear physics since 1963 [13]. A similar approach was adopted by Hal O. Anger, who in 1953 developed a whole-body rectilinear scanner made of a linear array of individual NaI(Tl) scintillation detectors supported by a structure able to move along the body of a patient [14].

The next step was the development of a large-area monolithic NaI(Tl) scintillation crystal whose readout is performed event by event by an array of PMTs.

An approach to improve spatial resolution consists in the segmentation of the scintillation crystal aiming to strongly reduce the spread of light distribution following the absorption of a γ-ray in the scintillator. Studies for upgrading the early prototypes of PET scanners were started in the 1980s. In particular, an array of BGO scintillation crystals, readout by four PMTs located at vertices of the light-output window of the array, were considered by Casey and Nutt for building a single block detector [15]. Setup of PET block detectors in the current commercial scanners is nowadays substantially unchanged, even if more effective block designs have been developed, based on arrays of scintillators coupled to PSPMTs [16]. Composite detectors based on an array of BGO crystals have been developed also for gamma cameras with SPECT capabilities [17].

6.7.4 Position-Sensitive Photomultiplier Tubes (PSPMTs)

The major steps toward the development of PSPMTs can be marked as (1) invention of the photoelectric tube in 1913, (2) development of the first PMT in 1930, and (3) development of the PMT with electrostatic focusing, the basic structure of current PMTs, in 1936.

The PSPMT still works according to the Anger principle, with the additional feature of using scintillation arrays with pixel bases less than 1 mm, thus potentially achieving submillimeter spatial resolution. Moreover, it is possible to choose low-cost geometries with optimized detection features for specific applications, e.g., for breast or brain imaging.

Furthermore, the compact design allows a reduction of shielding weight; for instance, for a 140 keV ^{99m}Tc energy γ-ray, a 20 × 20 cm FOV camera requires about a 12 kg weight lead shielding. Table 6.1 compares the main characteristics of the three generations of Hamamatsu PSPMTs [2], while Table 6.2 summarizes the main physical characteristics and operating features of initial prototype imaging probes based on inorganic scintillators and PSPMTs.

6.7.4.1 First-Generation Hamamatsu PSPMTs

The first 3″ PSPMT (model R2486 developed in 1985) was based on proximity mesh dynode; thereby, the charge was multiplied around the position of the light photon striking on the photocathode. Figure 6.11 schematizes the dynode structure of such PSPMT with the whole internal multiplication electrodes setup. In this PSPMT, the charge cascade was affected by a wide intrinsic spread. A number of factors affect such spreading, such as the interstage voltage of dynodes (in particular between cathode and first dynode), additional focusing grids between dynodes, and finally the intrinsic spreading of the light spot due to the photocathode

Table 6.1 Main characteristics of the three generations of Hamamatsu PSPMTs

Parameter	3″ R2486	5″ R3292	R5900-M64	R7600-C8/C12	Flat panel
Generation	First	First	Second	Second	Third
Window thickness (mm)	3.2	6	1.5	0.8	2.8
Dynode structure	Proxi mesh	Proxi mesh	Metal channel	Metal channel	Metal channel
Dynode number of stages	12	12	12	11	12
Anodes structure	Crossed wire	Crossed wire	Multi-anode	Crossed plates	Multi-anode
Number of anodes	16 + 16	28 + 28	64 (8 × 8)	4 + 4/6 + 6	64 (8 × 8)[a] 256 (16 × 16)[b]
Pixel size/pitch (mm)	3.75	3.75	2/2.25	5/5.5/3.6	5.6/6.0[a] 2.8/3.0[b]
Active area (mm)	50 Ø	100 Ø	18.1 × 18.1	22 × 22	49 × 49
Outer area (mm)	76 Ø	132 Ø	26 × 26	26 × 26	51.7 × 51.7
PMT thickness (mm)	55	113	20.1	20.1	15.5
Intr. charge spread (FWHM, mm)	7	11	<1	<1	<1
Packing density (%)[c]	43	57	48	71.6	90
Cathode luminous sensitivity (mA/Lm)	80	80	70	70	80
Gain	10^5	10^5	3×10^5	7×10^5	3×10^6
Anode dark current (nA)	20	40	12.8	2	96
Transit time (ns)[d]	17	–	5	5	5
Uniformity among anodes	1:4	1:4	1:5	1:4	1:3

[a]H8500 model
[b]H9500 model
[c]Effective area/outer size
[d]Time response

Table 6.2 Main characteristics and applications of prototype imaging probes based on inorganic scintillators and PSPMTs

Scintillator and size (mm)	PSPMT	Lead collimator, specifications[a]	Spatial resolution[b] (FWHM)	Imaging test
NaI(Tl) 60 × 60 × 4 thick	R2487 76.2 square	LEHR, 25.4 mm thick, Ø 0.1 mm holes, 0.02 mm septa	2.0 mm 140 keV	Guinea pig lungs and heart
NaI(Tl) 3 thick	R2487 76.2 square	Diverging holes, 13 mm thick, Ø 1.3 mm, 18° half angle	2.5 mm for ^{99m}Tc 4.0 mm for ^{111}In	Rat bone scan
CsI(Tl) Ø 50 × 0.5	R2486 Ø 76.2	Pinhole 0.5 mm	1.0 mm for ^{99m}Tc	Rat cerebellum
NaI(Tl) 76.2 × 76.2 × 5	R3292 Ø 125	Parallel-hole LEHR	2.5 mm 122 keV	Thyroid phantom
YAP(Ce) 11 × 22 array 0.6 × 0.6 × 7 thick	R2486 Ø 76.2	Pinhole 0.5 mm	0.7 mm for ^{99m}Tc	0.4 mm collimated source
CsI(Tl) Ø 50 × 0.5	R2486 Ø 76.2	Pinhole 0.5 mm	1.0 mm for ^{99m}Tc	Guinea pig brain
NaI(Tl) 73 × 73 × 8	R2487 76.2 square	Square parallel holes, 21.5 mm high, 1.2 mm pitch, 1.02 mm opening	2.4–3.8 mm for ^{99m}Tc	500 g rat, child hand
CsI(Tl) 16 crystal linear array 1.25 × 1.25 0.25 septa	R2487 76.2 square	Flood fields: 22.1 (keV) 32.1 59.5 122	4.5 mm 3.5 mm 1.9 mm 1.3 mm	Commercial baggage scanning
NaI(Tl) Ø 50 × 1.0	R2486 Ø 76.2	–	1.0 mm	Green plant

[a]*LEHR* Low-energy high-resolution
[b]*FWHM* Full width at half maximum

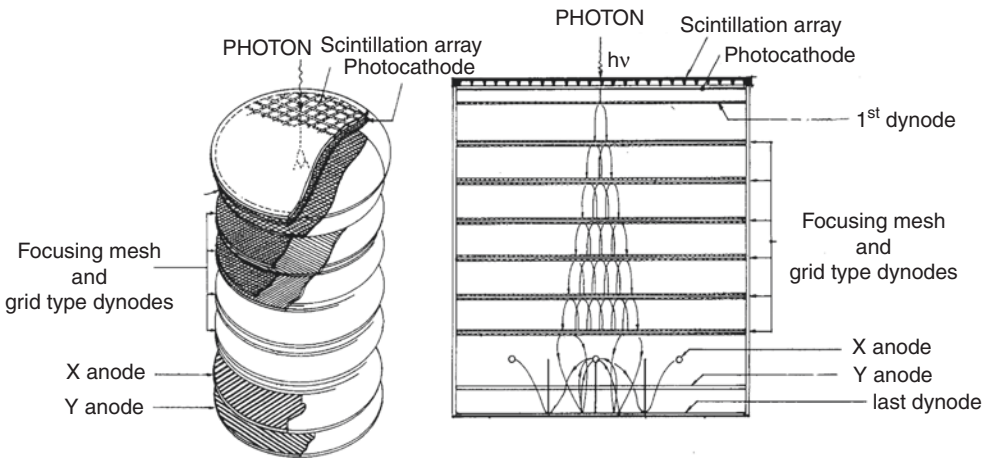

Fig. 6.11 Diagrammatic representation of the charge multiplication setup used by Hamamatsu Photonics for first-generation PSPMTs

optical glass window. Typical charge spreads are 9 mm and 14 mm FWHM for a 3″ and a 5″ PSPMT, respectively [18].

Such intrinsic wide charge spreading favors the use of crossed-wire anodes and the centroid method for position determination, rather than application as hodoscope where pixelated anodes with minimum crosstalk are required. Furthermore, a wide intrinsic charge distribution can limit the spatial resolution values of small light spots.

The first-generation PSPMT (which is housed in glass) is characterized by a large active area (5″ in diameter), which is useful for applications in physics, but is not large enough for medical imaging, where a 20 cm FOV is required even for small organs such as the thyroid, breast, or brain. Unfortunately, because of the quite large dead zone at the edge of this PSPMT (1 cm or more), it is not possible to assemble arrays of tubes as in the Anger camera.

Figure 6.12 compares first- and second-generation Hamamatsu PSPMTs. Models R6870 (8″), R3292 (5″), R5900 (1″ square), and R2486 (3″) are shown from left to right. A 3.5” floppy disk and a BNC adapter are shown in foreground and on the right of the R5900 PSPMT, respectively, for size comparisons (the R2486 PSPMT is represented with a reduced scale). The major limitation of the large-area, 8″ PSPMT (about 20 cm) was thickness of the

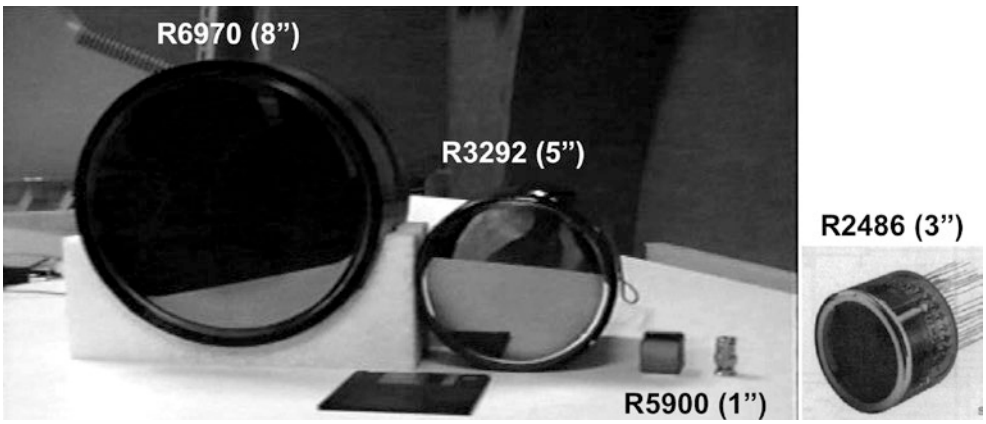

Fig. 6.12 Hamamatsu PSPMT models belonging to first and second generations (*reproduced from: Pani R, Pellegrini R, Soluri A, De Vincentis G, Scafè R, Pergola A. Single photon emission imaging by position sensitive PMT. Nucl Instr & Meth A 1998;409:524-8, Figure 2*)

photocathode glass window (7.5 mm), which produces further broadening of the light spot on the photocathode and, as a consequence, on the intrinsic spread of charge.

6.7.4.2 Second-Generation Hamamatsu PSPMTs

The second-generation PSPMT was based on metal channel dynode technology for charge multiplication, combined with a photocathode glass window less than 1 mm thick. The intrinsic light spread was then reduced down to 0.5 mm FWHM. The new dynode structure consists of electron multiplier layers that channel the charge, thus saving the position of the light spot interacting on the photocathode. The charge is collected by a multi-anodic structure made of an array of anodes lying on the same plane or a crossed-plate lying on two parallel planes for X and Y charge collection. Contrary to the first generation, the narrower charge distribution potentially increases the required number of anodes for optimum light sampling [19]. The Philips XP1700 PSPMT series was never commercialized with optimized peripheral dead zone, and Hamamatsu Photonics has remained the only corporation actively working in this field.

The intrinsic charge spread produced during the multiplication process slightly amplifies the scintillation light distribution at the photocathode, and a 1-mm-thick anode could be redundant and thus involve an oversampling of light distribution and useless additional readout electronics. Hamamatsu R7600-C12 series (6X + 6Y crossed-plate anodes) and R5900-M64 series (8X × 8Y anode array) have anode granularity well optimized, to 3 mm and 2.25 mm, respectively. Such light sampling size allows good identification of scintillation crystal pixels with side as small as 1 mm (C12) or less (M64), without relevant image distortions for 140 keV γ-rays. Finally, the adoption of a metal housing allows very compact size (about 1 in.^{3}) and reduction of the peripheral dead zones down to 2 mm.

A novel gamma camera, based on multiple assembly of 1″ PSPMTs of second generation, was proposed in 1997 [20]. Advantages of this novel camera include a reduced overall photocathode glass window thickness (0.8 mm) and the extensible detection area with regular or irregular shapes during the camera design. On the other hand, the relevant fraction of non-active area (30%) requires the use of an additional light guide (usually 3 mm thick) to allow detection in dead zones between neighboring photodetectors and reduction of light loss. This partially reduces the high imaging performance of individual PSPMTs.

Figure 6.13 shows two prototypes of detectors for small FOV gamma cameras based on assemblies of 4 × 4 (left) and 6 × 7 (right) Hamamatsu second-generation R7600-C12 PSPMTs. The corresponding FOVs are about 10 × 10 cm (100 cm^2) and 15 × 18 cm (270 cm^2), respectively, suitable for optimized anatomical fitting for specific organ imaging.

6.7.4.3 Third-Generation Hamamatsu PSPMTs

The third generation started with the H8500–H9500 Flat Panel PSPMT families [21]. The major advance is represented by housing that compacts a 2″ active area with the narrowest dead boundary (<1 mm), thus assuring a fraction of active area >80%. These Hamamatsu models use the same metal channel dynode technology and collect the charge with 8 × 8 or 16 × 16 anode array, respectively. With a photocathode glass window thickness of 2 mm, the H8500 family model would correctly sample the light spread produced by a 2 × 2 mm scintillation array. In order to clearly identify the pixels of a scintillation array with 1 × 1 mm crystals, the optimum anode size would be 3–4 mm, as in the case of the H9500 Flat Panel PMT family. This would compensate the worse spatial resolution due to the glass window thickness with a better position linearity.

Figure 6.14 shows the miniaturization steps from a large detection area first-generation Hamamatsu 5″ PSPMT (model R3292 on the right) to a third-generation H8500 Flat Panel (left, an array of 2 × 2 tubes is shown). The multiplication structure is visible through the broken glass of R3292. Overall, glass window areas are of about 127 cm^2 (R3292) and 103 cm^2 (array of 2 × 2 H8500 tubes). The flat panel

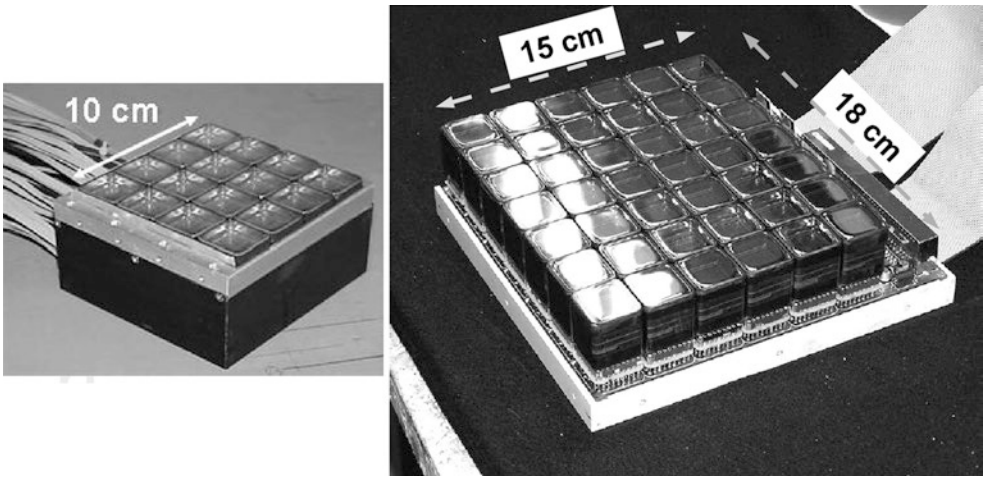

Fig. 6.13 Two prototypes of multiple-crystal small FOV gamma cameras based on assemblies of 4 × 4 (left) and 6 × 7 (right) Hamamatsu second-generation PSPMT model R7600-C12

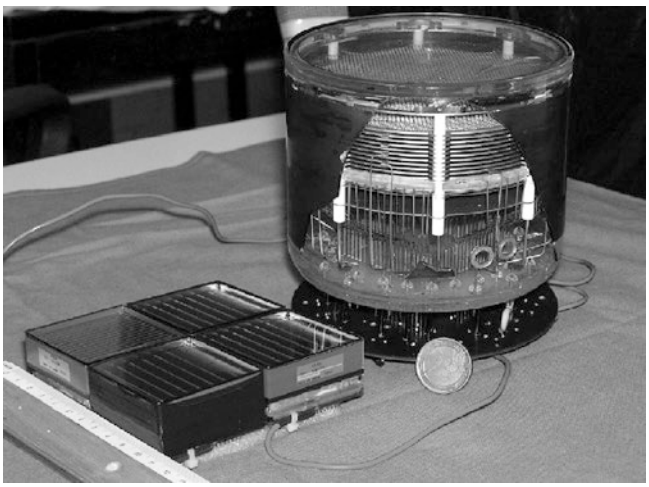

Fig. 6.14 Miniaturization steps for large detection area Hamamatsu PSPMT from first-generation 5″ Ø R3292 model (right) to third-generation H8500 Flat Panel (left, an array of 2 × 2 tubes is shown). The multiplication structure is visible through the broken glass of R3292. Overall glass window areas are of about 127 cm^2 (R3292) and 103 cm^2 (array of 2 × 2 H8500 tubes). HV-printed circuit boards are shown at respective bottoms. A 2-EUR coin is included in the picture for size reference

PMT is designed to overcome the limitation affecting the prior PSPMT generations. In fact, it can be assembled in arrays with an improved effective area up to 97% and a photocathode glass window thickness down to 2.8 mm.

An additional anode configuration made of 16X + 16Y crossed-plate, similar to the former model R5900-C8, has recently been proposed. Among the advantages of the crossed-plate layout with respect to the individual anodes, one can note a dramatic lowering of readout electronics (32 channels for 16X + 16Y versus 256 channels for 16X × 16Y) and a relevant reduction in the spatial density of pins in the PMT base (1.6 pin/cm^2 for 16X + 16Y versus 9.8 pin/cm^2 for 16X × 16Y). This configuration overcomes the limitations to the improvement of anodic granularity due to the electrical connections constraints [22].

6.7.5 Geiger-Mode Avalanche Photodiodes (G-APD)

The G-APD can be defined as a solid-state device able to detect a single light photon emitted under illumination [23]. It should be noted that the properties of such solid-state detectors have mainly been explored in the field of telecommunications, because PMTs used for fiber-optic coupling transmission have been burdened by important drawbacks for applications in medical imaging, e.g., gain instability and high cost. Nevertheless, the high-cost issue and other limitations have been addressed with the latest generation G-APDs, which can currently be utilized for compact gamma cameras as well as for PET/MR instrumentation, with some advantage with respect to conventional detection devices.

Key Learning Points

- Dedicated gamma cameras developed for specific applications fall into three categories: (1) semiconductor detectors in which the γ-rays interact directly with a position-sensitive solid-state detector; (2) scintillation crystals coupled to an array of solid-state photodetectors; or (3) scintillation crystals coupled with a position-sensitive photomultiplier tube.
- Compact gamma cameras with high spatial resolution can be assembled.
- Smaller devices scaled down to intraoperative dimensions have been successfully developed as imaging probes for use during radioguided surgery.
- Different materials are used for either scintillation detectors or semiconductor detectors.
- Small field-of-view imaging probes based on position-sensitive photomultiplier tubes have been developed.

6.8 Single-Photon Emission Mammography (SPEM)

Diagnosis and treatment of cancer at an early stage of development improve long-term outcome [2]. For breast cancer, X-ray mammography currently constitutes the main method of early cancer detection; however, its diagnostic accuracy is suboptimal, and many patients undergo unnecessary biopsies. Some of the equivocal/inconclusive findings of mammography can be clarified by exploiting the tumor-seeking properties of scintimammography (SM) with ^{99m}Tc-Sestamibi [24, 25]. As originally described by I. Khalkhali in 1993 [24], prone scintimammography (PSM) consists in positioning the detection head of a standard gamma camera in vertical position, lateral and as close as possible to the body, with the patient in prone position and the breast hanging. Although the initial results were encouraging, there was a critical detection limit for breast lesions smaller than 1 cm in diameter. Reduced sensitivity for smaller cancers is mainly due to the inadequate positioning capability of a standard gamma camera head, which is too bulky for optimal breast imaging. In particular, inadequate spatial resolution (typically 3 mm) and the fact that major portions of the breast are positioned at a distance >5 cm (and up to 15 cm) from the collimator surface dramatically reduce breast lesion contrast in PSM [26].

On the other hand, as shown in Fig. 6.15, a dedicated imager can easily reduce the breast-to-collimator distance, thus increasing the sensitivity of SM for lesions much smaller than 1 cm in size, such as T1a and T1b cancers. In this regard, it was shown that use of a small FOV gamma camera with very high intrinsic spatial resolution (1.7 mm), located closer to the tumor by breast compression, results in increased sensitivity (up to 80%) for tumors ≤1 cm in size, without apparently reducing specificity [27, 28]; nonetheless, the results remained unsatisfactory for smaller lesions (T1a). It should be emphasized that SPEM with the new small FOV detectors allows acquisition of scintigraphic images in similar views and operating conditions (breast compression) as during X-ray mammography.

Over the last two decades, several prototypes for SPEM imaging based on PSPMT technology and pixelated CsI(Tl) scintillation crystals have been developed. Cameras with about 11 cm in diameter useful FOV have been described, with spatial resolution around 2–3 mm when the camera is in contact with the source object—as it occurs for imaging during breast compression [29] (Fig. 6.16). Furthermore, mild compression of the breast allows separation of overlapped objects that would otherwise not be distinguished during PSM with a standard gamma camera (Fig. 6.17). The efficacy of breast compression optimal imaging parameters is shown in Fig. 6.18, where the respective spectra are plotted. The large tumor size combined with the large variations in breast thickness (4.5 cm) shows an impressive increase of counts in the specific energy peak with respect to the broad Compton peak.

In early prototypes, the relatively small FOV limited optimal imaging of the breast. To overcome this limitation, novel gamma camera has been proposed based on the Anger principle, but replacing conventional PMTs with compact PSPMTs. Larger prototypical modular gamma cameras, made of up to a 7 × 8 array of 1″ PSPMTs, have been developed worldwide by different research groups. In this way, it was possible to exploit the narrow scintillation light distributions, recovering at the same time the position information for events falling in the dead space between neighboring PMTs. The main advantages of such modular design are (1) minimum detector thickness (<3 cm), (2) light weight, (3) small dead boundary zone (3 mm), and (4) no limitation in the active area shape and size.

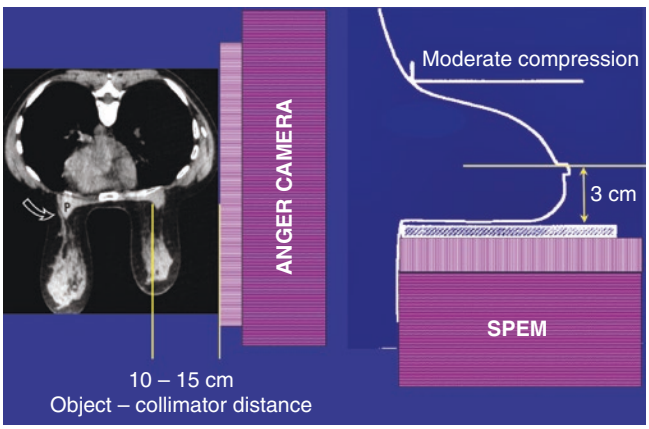

Fig. 6.15 Main geometric arrangements for prone scintimammography (PSM, left) and single photon emission mammography (SPEM, right) (*reproduced from: Garibaldi F, Cisbani E, Cusanno F, Iommi R, Urciuoli GM, Pani R, Pellegrini R, Scafè R, Indovina L, Cinti MN, Trotta G. Optimization of compact gamma cameras for breast imaging. Nucl Instr & Meth A. 2003;471:222-8, Figure 1 (a,b)*)

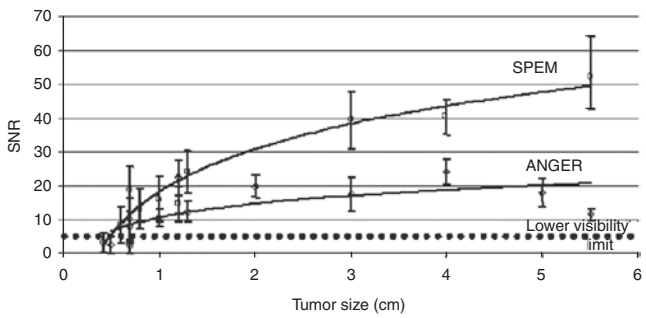

Fig. 6.16 Plot of the signal-to-noise ratio (SNR) values as a function of tumor size, obtained from clinical measurements made with a SPEM camera in cranio-caudal view and with an Anger camera (lateral view of the body, with the patient in prone position and the breast hanging), respectively (*reproduced from: Pani R, Pellegrini R, De Vincentis G, Cinti MN, Weinberg IN, Soluri A, et al. Factors affecting cancer detectability in Tc-99m MIBI scintimammography. Nucl Instr & Meth A. 2003;497:90-7, Figure 2*)

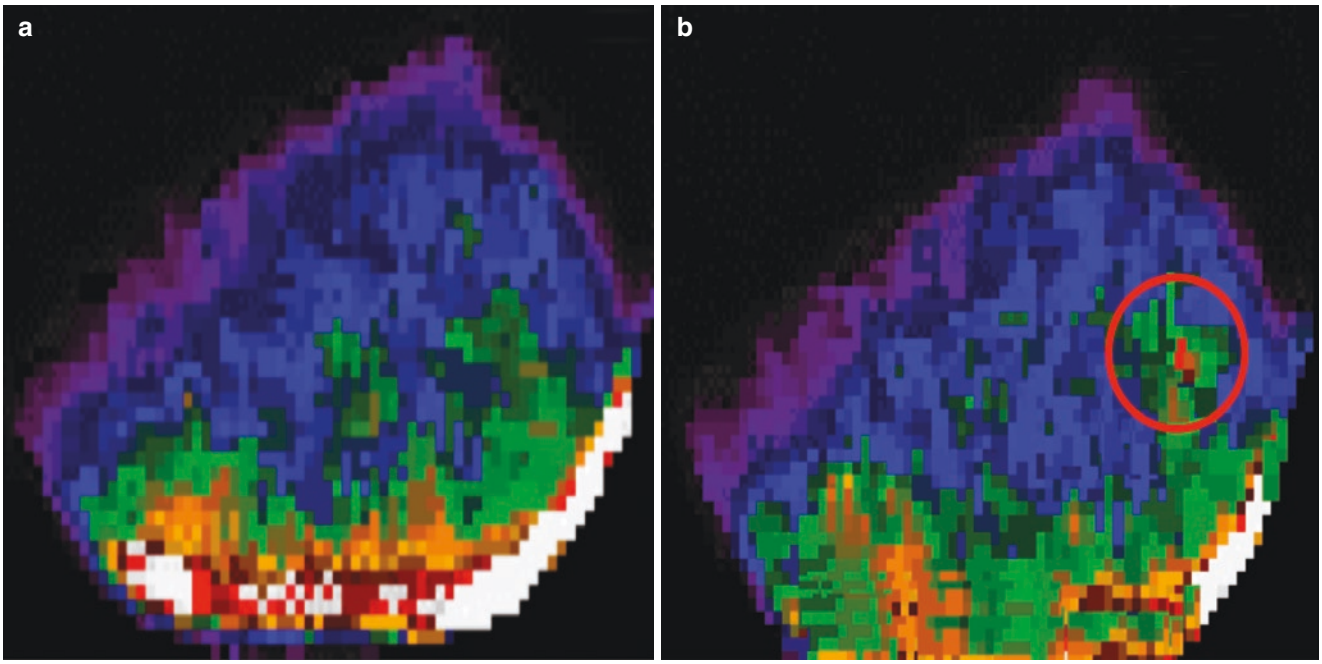

Fig. 6.17 Right breast carcinoma, 7 mm in size: ^{99m}Tc-sestamibi images obtained with a SPEM camera without breast compression (**a**) and with mild breast compression (**b**). Mild compression results in better definition of the lesion as an area with increased tracer uptake (red circle) (*reproduced from: Pani R, Pellegrini R, De Vincentis G, Cinti MN, Weinberg IN, Soluri A, et al. Factors affecting cancer detectability in Tc-99m MIBI scintimammography. Nucl Instr & Meth A. 2003;497:90-7, Figure 4*)

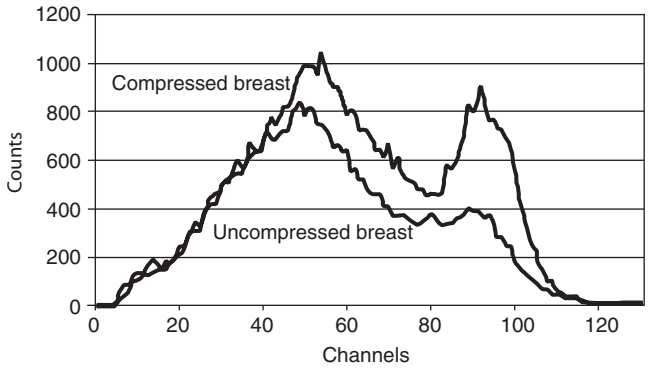

Fig. 6.18 Energy spectra for the same tumor (4.5 cm in size) acquired with and without mild breast compression (*reproduced from: Pani R, Pellegrini R, De Vincentis G, Cinti MN, Weinberg IN, Soluri A, et al. Factors affecting cancer detectability in Tc-99m MIBI scintimammography. Nucl Instr & Meth A. 2003;497:90-7, Figure 5*)

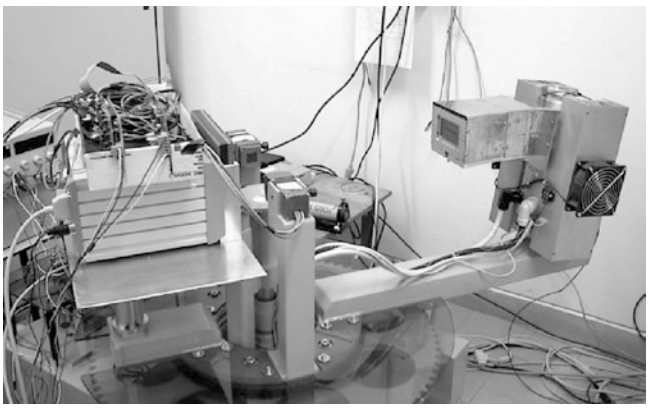

Fig. 6.19 Prototype of a breast-dedicated SPECT/CT scanner (*reproduced from: Gambaccini M, Fantini A, Bollini D, Castelli E, Del Guerra A, Di Domenico G, et al. Development of a quasi-monochromatic CT system for breast cancer study with combined emission-transmission tomography. IEEE Trans Nucl Sci. 2001;48:703-6, Figure 2*)

A compact-design combined SPECT/CT imaging camera has also been proposed to overcome the limitations of poor specificity for stand-alone X-ray mammography and poor sensitivity of SM [30] (Fig. 6.19). The reconstructed images strongly enhanced scintigraphic contrast for tumors <1 cm in size with respect to planar geometry. These results demonstrate the feasibility of exact 3D localization of tumor lesions using single-photon compact ring tomography combined with X-ray transmission tomography.

Commercial cameras for SM, currently better identified as "breast-specific gamma imaging" (BSGI) or "molecular breast imaging" (MBI), are mostly based on solid-state detector technology. Both single-head and dual-head BSGI are available, with useful FOV up to 16 × 20 cm. Intrinsic spatial resolution using tungsten collimators is generally better than 2 mm, with energy resolution values around 5% (FWHM) for 140 keV photons (the typical γ-ray emission of ^{99m}Tc). Mild breast compression is performed during scintigraphic acquisition, and the detector(s)

Fig. 6.20 Setup of a commercial breast-dedicated gamma camera that can be equipped with either one or two revelation heads based on CdZnTe detectors. Mild breast compression is performed by adjusting the distance between the two detectors (or between the single detector and the opposing breast holder) according to size of the breast in the individual patient. The detector(s) can be positioned in any position to acquire scintigraphic views mimicking the projections adopted for X-ray mammography, from orthogonal to oblique; an oblique view is shown here (*image downloaded from "www.cmr-naviscan.com/lumagem/"*)

can be rotated to replicate the standard orthogonal and oblique views/projections as during X-ray mammography, thus facilitating comparisons between the two sets of images (conventional mammography and BSGI/MBI) (see Fig. 6.20).

Key Learning Points

- The signal-to-noise ratios obtained by SPEM acquired during mild breast compression are greater of about a factor two versus the corresponding value obtained during scintimammography.
- SPEM with breast-dedicated gamma cameras can efficiently visualize tumors less than 1 cm in size, with signal-to-noise ratios ranging from 7 to 20.
- Mild breast compression allows discrimination of overlapped lesions.

6.9 Cardiac-Dedicated Gamma Cameras

When employed for cardiac SPECT studies, conventional gamma cameras generally utilize two scintillation detectors fixed at a 90° angle to one another; some (older generation) gamma cameras are also equipped with adequate radioactive sources for transmission imaging-based, patient-specific attenuation correction. Due to the left anterior position of the heart in the chest, cardiac SPECT imaging typically involves acquisition of projection data over only a 180° orbit (instead of the 360° orbit used for general SPECT imaging)—from right anterior oblique to left posterior oblique. By positioning the two detectors at a 90° angle, the two detectors can simultaneously acquire usable data over the 180° orbit; if the two detectors were in the usual opposed position (180°), only one of the two detectors would actually acquire usable data. Dedicated cardiac SPECT scanners with two scintillation detectors fixed at a 90° angle have been built by Philips (CardioMD™) and by Siemens (CCam™).

Siemens has also introduced the so-called "cardio-focal" (SmartZoom™) field-upgradeable collimators for high-sensitivity cardiac imaging with conventional dual-head gamma cameras [6, 7]. Also known as "astigmatic" collimation, in such converging/diverging collimator, the converging collimation magnifies the central FOV in both the axial and transaxial directions, while the diverging collimation minifies the periphery of the FOV to provide coverage of the entire body (Fig. 6.21), thereby avoiding truncation artifacts commonly seen with fan-beam collimators when imaging the torso. Such cardio-focal collimators increase sensitivity for cardiac imaging by a factor of approximately two compared to high-resolution parallel-hole collimators.

The Digirad Cardius 3 XPO™ cardiac scanner employs three pixelated CsI(Tl) scintillation detectors and images the patient in an upright seated position (Fig. 6.22); one- and two-detector Cardius systems are available as well. The system uses fan-beam collimators in the three-detector configuration coupled to photodiode detectors. The two outer detectors are positioned at a 67.5° angle relative to the central detector. Data is acquired by rotating the chair (rather than detectors) by 67.5°, yielding an overall acquisition arc of 202.5°. Its SPECT spatial resolution (FWHM) is 11.0 mm (radius of rotation: 20 cm) and sensitivity 160 cpm/μCi for ^{99m}Tc using LEHR collimation.

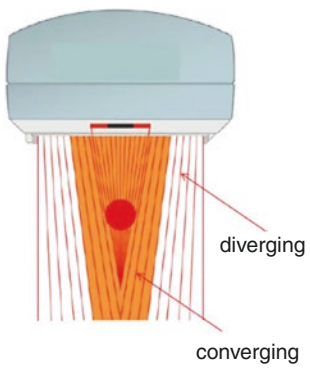

Fig. 6.21 Data acquisition geometry with the Siemens SmartZoom™ cardio-focal (diverging/converging) collimator. It provides higher sensitivity in the heart region by selective maximal magnification of that region (*reproduced from: Slomka PJ, Berman DS, Germano G. New cardiac cameras: single-photon emission CT and PET. Semin Nucl Med. 2014;44:232–51*)

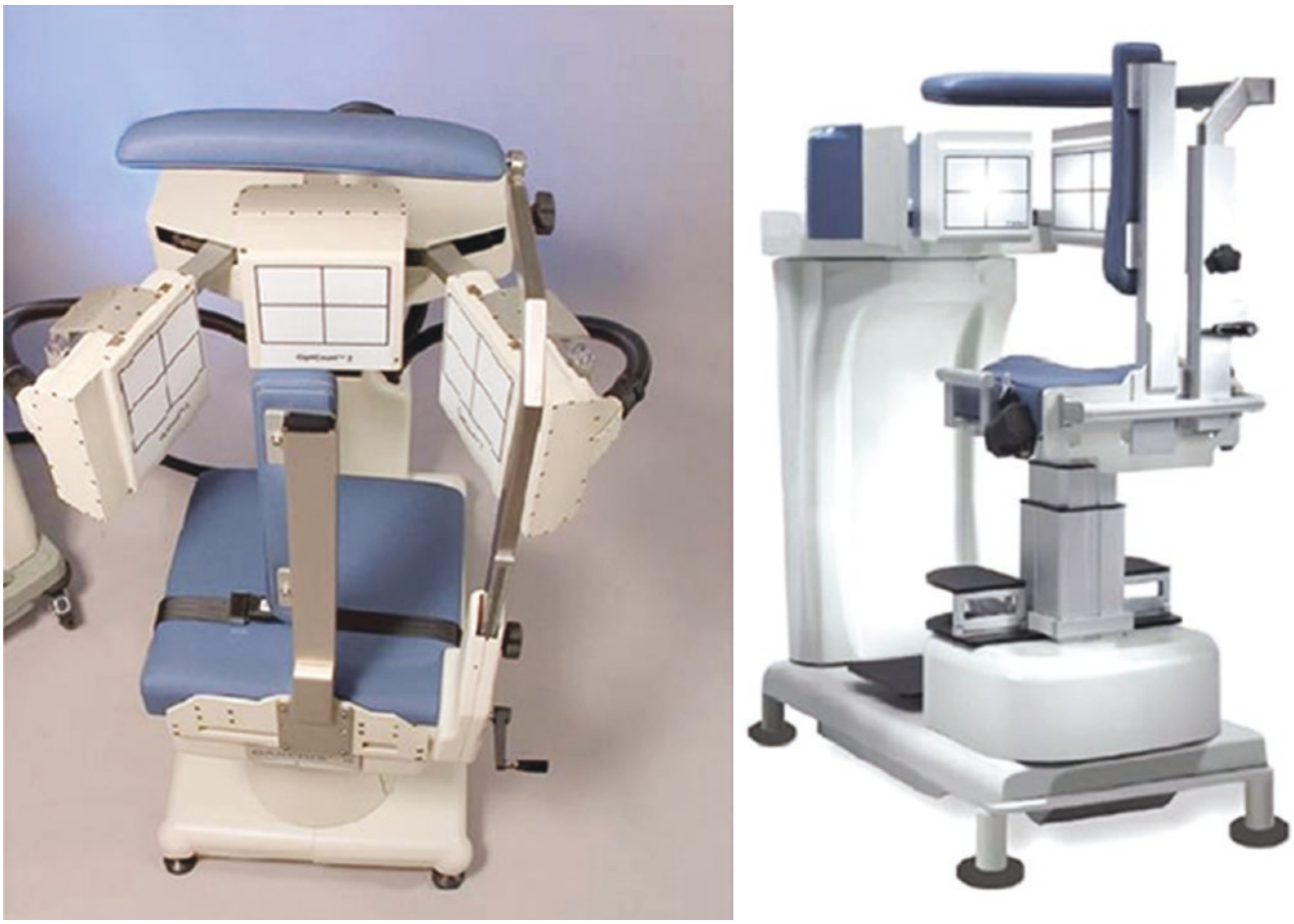

Fig. 6.22 The Digirad Cardius 3 XPO™ system. The patient is seated upright, and the chair rotates to achieve the required angular sampling (*reproduced from: Slomka PJ, Berman DS, Germano G. New cardiac cameras: single-photon emission CT and PET. Semin Nucl Med. 2014;44:232–51*)

The Digirad Cardius X-ACT™ system augments the Cardius 3 XPO™ features by adding a fan-beam X-ray source for CT imaging. The CardiaArc HD-SPECT™ [31] also images patients in an upright seated position. It is constituted of three curved stationary NaI(Tl) crystals backed by three rows of 20 PMTs, with a thin curved-lead collimator (the so-called aperture arc) having six vertical slots for horizontal collimation and rotating slowly back and forth every 10 s. Spatial resolution of CardiaArc™ is 3.6 mm at an 82 mm source-to-detector distance and 7.8 mm at a 337 mm source-to-detector distance.

Two vendors have introduced CdZnTe-based cardiac SPECT systems. The Spectrum Dynamics D-SPECT™ utilizes pixelated CdZnTe detector arrays mounted in nine vertical columns, with four detectors in each column, positioned in a 90° gantry geometry (Fig. 6.23). Each column consists of an array of 1024 CdZnTe elements (2.46 × 2.46 × 5 mm thick) arranged in a 16 × 64 element array with a size of 40 × 160 mm, achieving 16 cm of coverage of the thorax. Each detector array is fitted with square-aperture, high-sensitivity, parallel-hole collimators such that the dimensions of each hole are matched to the size of a single detector element. Spectrum Dynamics also recently introduced a less expensive six-detector column system. In another CdZnTe-based camera design developed by General Electric (Discovery NM 530c™ and Discovery NM/CT 570c™), a curved array of 19 5-mm-thick CdZnTe pixelated detector arrays is employed, each with a focused pinhole collimator (Fig. 6.24). Each detector array consists of four detectors, each with 246 CdZnTe detector elements (2.46 × 2.46 × 5 mm thick) arranged in a 16 × 16 element array. In these two systems, the detector gantry does not rotate or otherwise move. The remarkably high sensitivity of these systems is not related to the intrin-

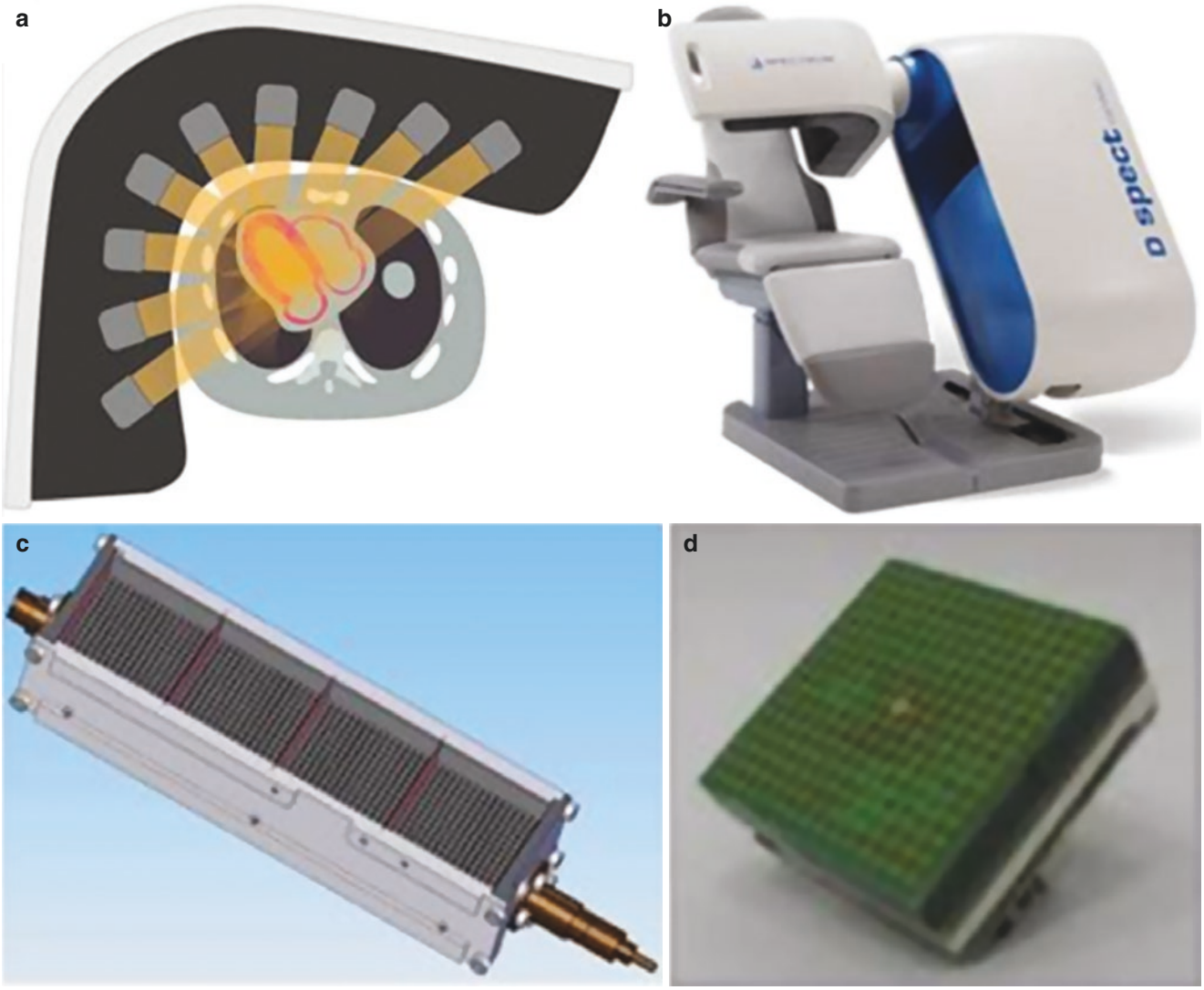

Fig. 6.23 Spectrum Dynamics D-SPECT™ system. (**a**) Detector configuration (top view) with the nine angularly directed detector blocks. (**b**) Photograph of the system. The patient may be seated upright, or the chair reclines so that the patient may lie nearly supine. (**c**) One of the nine detector blocks. (**d**) One of the CdZnTe detectors (*reproduced from: Slomka PJ, Berman DS, Germano G. New cardiac cameras: single-photon emission CT and PET. Semin Nucl Med. 2014;44:232–51*)

sic sensitivity of the CdZnTe detectors, but rather to the high-sensitivity geometric arrangement and collimation of the detectors.

The above cardiac-dedicated cardiac scanners provide higher sensitivity (up to sevenfold) and better spatial resolution than conventional gamma cameras, as illustrated in Fig. 6.25. Imaging times with these scanners thus range from 2 to 3 min for systems with solid-state detectors and 4 min for scintillation-detector systems with cardio-focal collimation.

Key Learning Points

- Cardiac-dedicated gamma cameras utilize special geometry of the detector head(s) to obtain tomographic images (SPECT) without having to perform detector head rotation.
- Cardiac-dedicated scanners provide higher sensitivity (up to sevenfold) and better spatial resolution than conventional gamma cameras.

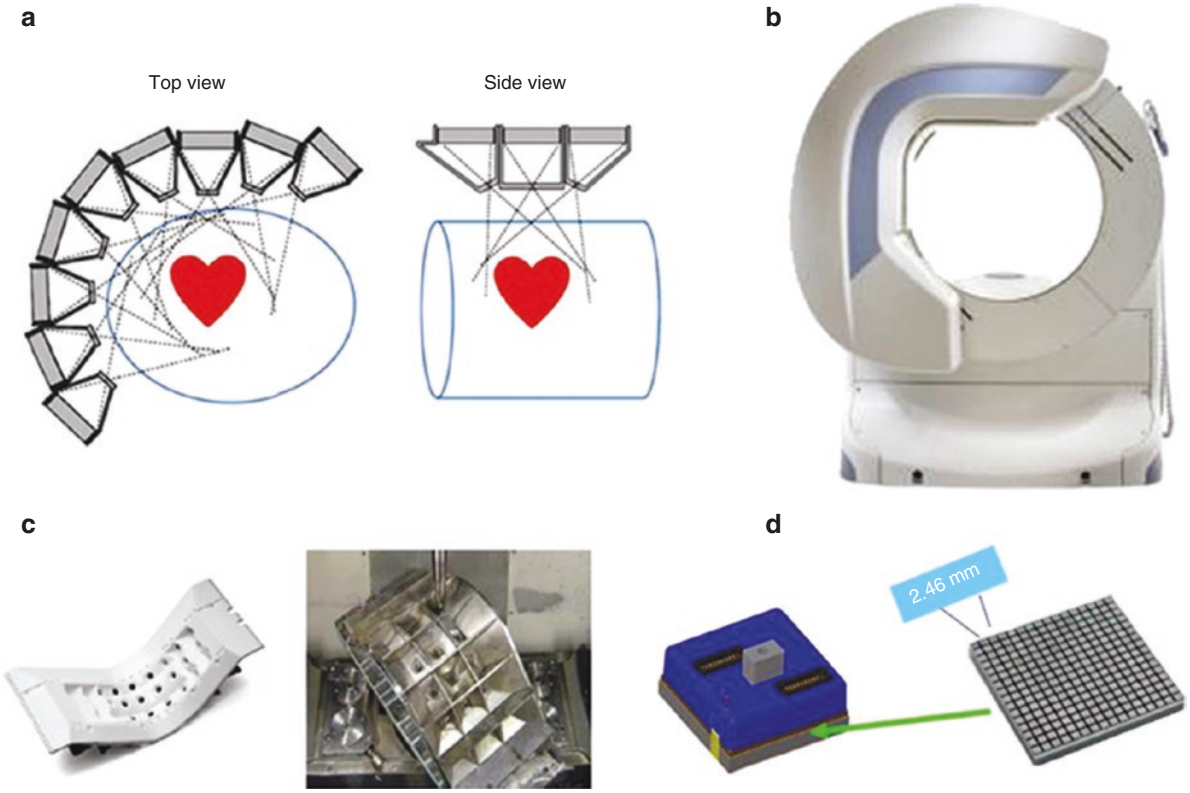

Fig. 6.24 General Electric NM 530c™ system with nine detector blocks arrays. (**a**) Detector configuration (top and side views). (**b**) Photograph of the system. The patient lies supine. (**c**) The pinhole collimation. (**d**) One of the CdZnTe detectors (*adapted from: Slomka PJ, Berman DS, Germano G. New cardiac cameras: single-photon emission CT and PET. Semin Nucl Med. 2014;44:232–51*)

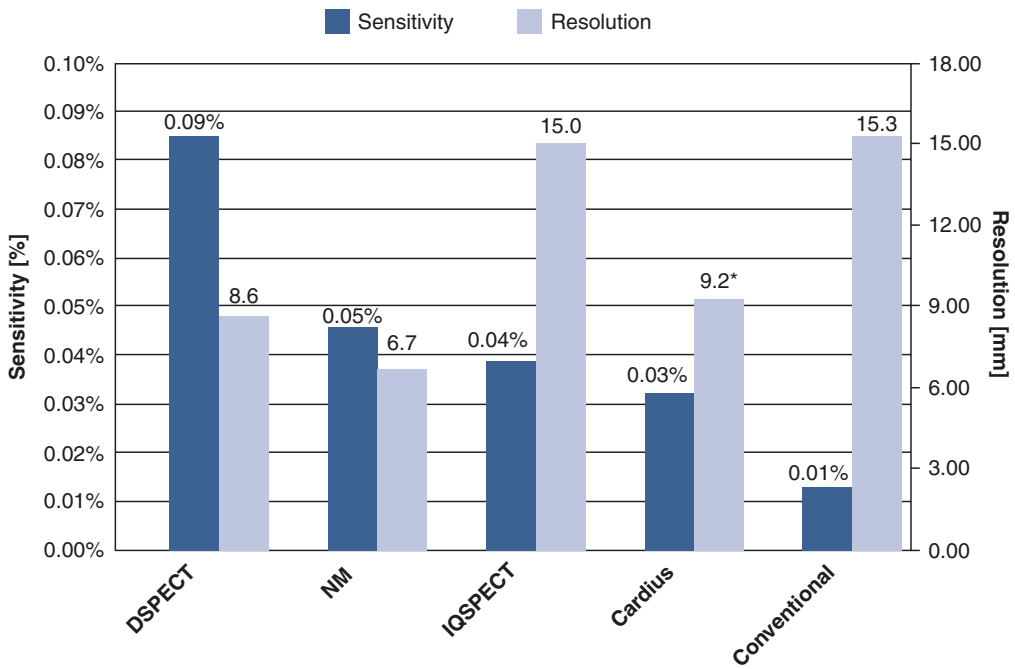

Fig. 6.25 Sensitivity in % (left axis) and reconstructed image resolution in mm (right axis) of dedicated cardiac SPECT systems compared to those of a conventional dual-head system. D-SPECT, Spectrum Dynamics D-SPECT™ system; NM, GE 530c/570c™ system; IQSPECT, Symbia system with dual-head Siemens SmartZoom™ cardio-focal (diverging/converging) collimators; Cardius, Cardius Digirad X•ACT™ system with fan-beam collimators; conventional, conventional dual-headed SPECT with low-energy high-resolution collimators (*reproduced from: Slomka PJ, Berman DS, Germano G. New cardiac cameras: single-photon emission CT and PET. Semin Nucl Med. 2014;44:232–51*)

6.10 Handheld Gamma-Probes for Radioguided Surgery

Handheld gamma-probes for radioguided surgery have been used since the late 1940s, constituted by Selverston-Robinson needle-shaped detectors (a Geiger-Müller-type device) employed to assess completeness of tumor resection after administration of ^{32}P-orthophosphate to patients with brain tumors [32].

At that time, the primary device available to count radioactivity in the earliest nuclear medicine applications was the Geiger-Müller (GM) tube, the basic radiation detector (together with the ionization chamber) used in nuclear plants. GM tubes were commercially available, particularly in miniaturized models, well suitable for ionizing radiation probes (Fig. 6.26).

After several years of apparent oblivion, new-design handheld gamma-probes for radioguided surgery became commercially available in the mid-1980s, initially operating as single-channel counting devices yielding a counting value (or range) of event rate and the corresponding audible/visible signals, whose intensity/color was modulated according to the count rate.

The family of single-channel, or counting, probes includes devices based on a plurality of physical principles for detection ionizing radiation, all of them basically providing a count-rate value in the examined region of interest, that can be explored in the open surgical field after administration of a diagnostic radiopharmaceutical suitable for accumulation/concentration and retention in the tumor lesion to be resected. The region to be explored may be delimited by the short range of radiations in the tissues, as in the case of the β^- particles emitted by ^{32}P detected by a GM-type tube (the earlier probe), or by a suitable collimator absorbing γ-rays, as in the currently available scintillation or semiconductors probes (Fig. 6.27).

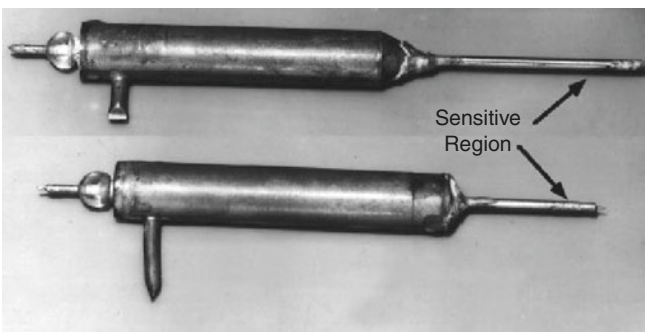

Fig. 6.26 Photograph of the earliest Geiger-Müller (GM) tubes used as intraoperative probes (Courtesy of Melvin Griem, MD, Professor Emeritus, University of Chicago, assistant to C. Robinson in 1948). The sensitive region is about 3 mm in diameter, and only about 1–1.5 cm at the tip is sensitive to radiation (*reproduced from: Hoffman EJ, Tornai MP, Janecek M, Patt BE, Iwanczyk JS. Intraoperative probes and imaging probes. Eur J Nucl Med. 1999;26:1913-35, Figure 1*)

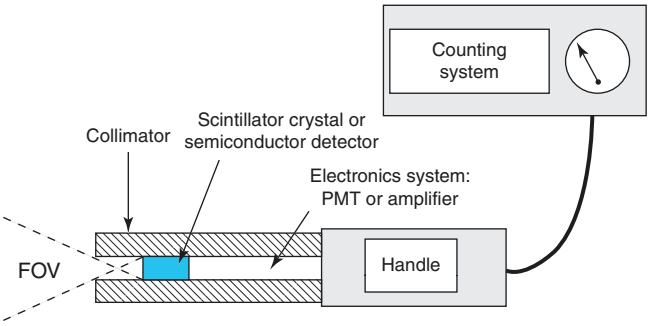

Fig. 6.27 Schematic of a traditional scintillation or semiconductor gamma-probe

6.10.1 Scintillation Probes

An early scintillation probe was developed in the late 1950s [33], based on the use of a CsI(Tl) crystal. The scintillation light output was read out remotely by using optical fibers or light pipes, because the available PMTs had a minimum diameter of 1" [34]. The light losses were reduced when reliable 10-mm-diameter PMTs became commercially available for more efficient gamma-probe assemblies, which also allowed better energy resolution and background rejection by pulse-height windowing [35].

The term "background" used during radioguided surgery does not refer to environmental radiation (as commonly referred to for conventional radionuclide imaging), but rather to the quantity of radioactivity present in the healthy tissues surrounding the target tissue to be resected. Design of the distal, radiation-sensitive portion of handheld gamma-probes for radioguided surgery is critical, as it must constitute the best design trade-off between absorption of background γ-rays by the collimator (depending on material and thickness) and its aperture that defines the probe sensitivity.

Furthermore, appropriate electronics must assure a coarse spectrometry (due to the poor energy resolution of the probe) for rejecting gammas scattered in the body and connects the selected signals to a rate meter, which produces audible signals and digital readouts.

6.10.2 Semiconductor Probes

Solid-state semiconductor detectors quickly replaced GM-like tubes in the few applications where miniaturization was required [36]. These detectors are characterized by good energy resolution in a very small size [35]. As an example of extreme miniaturization, Lauber developed a single detector placed inside a needle of 1.1 mm in diameter, as well as an array of multiple detectors arranged inside a needle with 1.5 mm diameter [37].

6.10.2.1 Cadmium Telluride Detectors

Due to the higher atomic number values of cadmium and tellurium ($Z = 48$ and $Z = 52$, respectively) with respect to silicon ($Z = 14$), CdTe detectors are better suited for low-energy γ-rays (e.g., 140 keV from ^{99m}Tc) than Si detectors, which are instead more appropriate for β^- detection [43].

Nevertheless, if interactions occur deeply in the detector, a fraction of ionization charge is not recorded, thus producing long tails at low energy of the photo peak with a relevant loss of energy resolution. Notwithstanding these limitations, CdTe (as well as CdZnTe and CdHgTe) are mostly used for probes at lower-energy photon detection, like those emitted by ^{125}I (27–37 keV, the ideal energy range for CdTe detectors). In these conditions, a very thin collimator can be highly effective and cheap.

Key Learning Points

- Single-channel (counting) probes include a wide category of devices based for detection of ionizing radiation, all substantially providing a count-rate value in the examined region/volume of interest.
- Handheld gamma-probes are employed intraoperatively for radioguided surgery.

6.11 Imaging Probes

Several applications of radioguided surgery, typically sentinel lymph node biopsy—especially if performed in intracavitary environments (e.g., during laparoscopic surgery)—are considering the use of dedicated imagers instead of a standard Anger camera or single-channel gamma-probes that only detect or count radioactivity. For image-guided surgery, a combined approach is generally adopted: (1) preoperative scintigraphy with a standard gamma camera, followed by (2) intraoperative use of a handheld counting gamma-probe. Several prototypes of miniaturized gamma cameras have been developed, based on the use of PSPMTs such as the second-generation Hamamatsu R5900-C8; these devices are called "imaging probes" (IPs) and are characterized by high resolution (around 2–3 mm FWHM, with 20% window centered on the 140 keV peak energy of ^{99m}Tc), full portability with light weight for intraoperative use, and a useful FOV of at least 1 in.^{2} [38, 39].

Early small FOV gamma cameras were based on inorganic scintillators coupled to 3″ or 5″ crossed-wire anode Hamamatsu PSPMT for scintillation light-output readout (Table 6.2). The setups generally involved monolithic crystals, although systems based on 2-D and 1-D [40, 41] achieved spatial resolution values of around 1 mm. In particular, Pani et al. used an array of 11 × 22 YAP(Ce) crystals, sized 0.6 × 0.6 mm, 7 mm high [40]. The array setup includes optical insulation between the crystals with 5-μm-thick reflective layers and is optically coupled with the R2486 Hamamatsu PSPMT. The final spatial resolution was about 0.7 mm at 140 keV. Instead, Truman et al. [41] used CsI(Tl) crystal arrays to develop a small FOV SPECT device with spatial resolution of 1.3 mm at 122 keV (extrapolated to 1.1 mm at 140 keV).

Key Learning Point

- Imaging probes are mostly used for small field-of-view imaging of the surgical bed, but not for actual intraoperative guide.

6.11.1 Generalities on the Use of Portable Probes for Radioguided Surgery

The use of portable probes (either single-channel counting probes or dedicated small FOV imaging probes) for radionuclide-based detection and localization of tumors, especially small tumors, has several well-known limitations [42], as follows:

- The absolute tumor uptake of tumor-seeking radiopharmaceuticals is generally quite low, typically ~0.1% or less of the administered activity per gram.
- The overall sensitivity of radiation detection in vivo is also quite low, ranging from about 0.1% for gamma camera imaging (including SPECT) to ~10% for PET.
- Such low counting efficiency is further exacerbated by the signal-degrading effect of attenuation of emitted radiation by overlying tissue.
- A significant fraction of the counts apparently emanating from a tumor or other targeted tissue may actually include counts originating elsewhere (i.e., from background activity in adjacent tissues) because of contrast- and resolution-degrading Compton scatter.

The above limitations can be mitigated, at least in part, through the use of intraoperative probes and, potentially, intraoperative gamma cameras. In fact, because of the close proximity that can be achieved at surgery between a collimated detector and the target tissue to be surgically resected (e.g., a tumor or a sentinel lymph node following their adequate preoperative radiolabeling), radionuclide detection of such structures can be enhanced using easy-to-handle intraoperative gamma-probes or small FOV, dedicated gamma cameras.

6.11.1.1 Gamma-Probes

The most widely used type of intraoperative probe (e.g., for sentinel lymph node detection) is the general-purpose gamma-

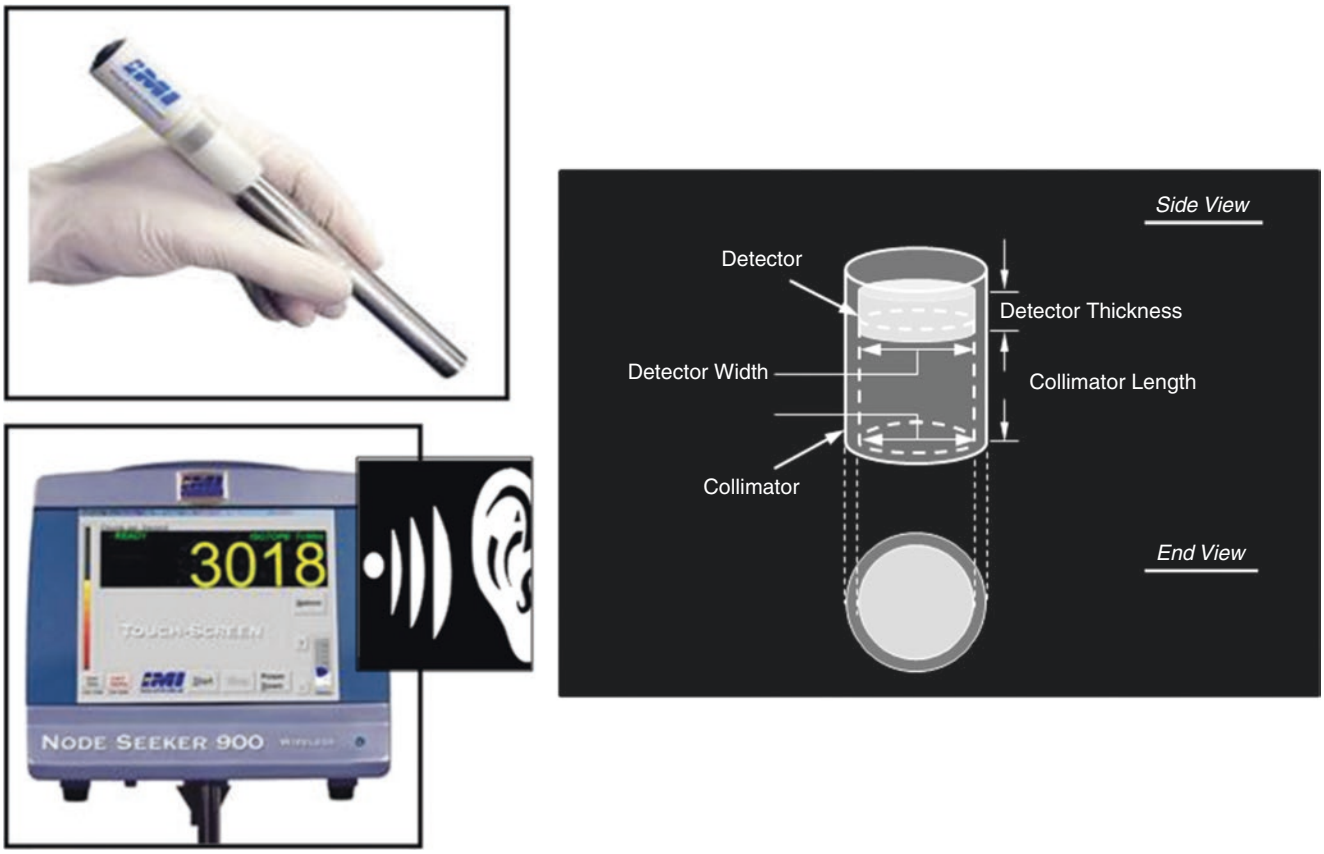

Fig. 6.28 The general design and operating principles of an intraoperative gamma-probe. The handheld probe (upper left panel) is comprised of a collimated, small-area (typically ~1 cm in diameter) scintillation or solid-state ionization (i.e., semiconductor) detector (right panel). The probe itself is connected to a control unit (lower left panel), which typically provides both a visual readout of the count rate and an audible signal related to the count rate, with the frequency of the latter signal increasing or decreasing in relation to the detected count rate

probe (Fig. 6.28), designed for counting local activity of radionuclides emitting X- and/or γ-rays; such single-photon emitters include ^{99m}Tc, ^{111}In, ^{123}I, and ^{131}I [43]. Gamma-probes generally use inorganic (i.e., non-plastic) scintillation detectors or solid-state (i.e., semiconductor) ionization detectors and lead or tungsten for shielding and collimation. Scintillators used in such probes include NaI(Tl), CsI(Tl), CsI(Na), and cerium-doped lutetium ortho-oxysilicate [LSO(Ce)]. Semiconductors used for intraoperative gamma-probes include CdTe, CdZnTe, and mercuric iodide (HgI_2).

Although scintillation detectors are characterized by high sensitivity, while the solid-state semiconductor detector allows better energy resolution (and therefore better scatter rejection), in the clinical routine use, the two types of probes generally provide comparable performance. Positron emitters such as fluorine-18 (^{18}F) may also be counted with such probes by single-photon (i.e., non-coincidence) counting of the 511 keV annihilation photons. However, as shown in Fig. 6.29, this requires thicker collimation and shielding to minimize penetration of such high-energy photons emitted from outside of the FOV (as defined by the collimator aperture) from reaching the detector and thereby degrading spatial resolution as well as target-to-background contrast [44, 45].

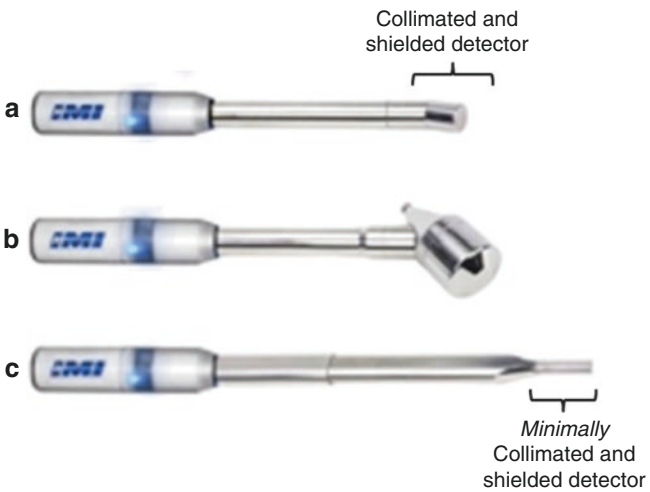

Fig. 6.29 Comparative thickness of gamma-probe collimation and shielding required for low- to medium-energy X- and γ-rays of single-photon emitters (**a**), for the high-energy (511-keV) annihilation γ-rays of positron emitters (**b**), and for negatrons and positrons of beta-particle emitters (**c**). Note the much thicker collimation and shielding required for counting of the annihilation photons and the minimal collimation and shielding for counting of beta-particles. Courtesy of IntraMedical Imaging, Los Angeles, CA (*reproduced from: Heller S, Zanzonico P. Nuclear probes and intraoperative gamma cameras. Semin Nucl Med. 2011;41:166–81*)

Beta-Probes

Since X- and γ-rays penetrate relatively long distances (of the order of 10 cm) of soft tissue, a major limitation of the use of gamma-probes to specifically identify the target tissue during radioguided surgery is the presence of variable, generally high levels of background activity in surrounding normal tissues. Thus, even with a gamma-probe positioned over the skin projection of a tumor, the contribution of counts originating from activity in normal tissue underlying the tumor and even outside the field of view (due to a certain degree of penetration of the collimation and shielding) may degrade the tumor-to-normal tissue contrast (e.g., reduce the tumor-to-normal tissue count ratios to less than 1.5:1 [44, 46] and thus tumor detectability to the point where lesions may be missed).

A potential solution to this limitation of radioguided surgery is the use of so-called beta-probes, that is, intraoperative probes which specifically yield counts of negatrons or positrons. Since they have very short ranges in soft tissues (typically of the order of 1 mm or less), the β particles emitted by activity outside the probe's FOV or underlying the surface tissue do not reach the detector and are not counted. By the same token, minimal if any collimation and shielding is required (Fig. 6.29c). Therefore, the discrimination between higher-activity tumor and lower-activity normal tissues is enhanced, and the tumor-to-normal tissue count ratios are increased. Of course, the very short range of beta-particles in water/tissues restricts the use of such probes to surface lesions; beta-probes could not be used, for example, for (percutaneous) detection of sentinel lymph nodes. Beta-probes generally utilize either semiconductor or plastic scintillator detectors, since such detectors have lower effective atomic numbers and mass densities than inorganic scintillators such as NaI(Tl) and lower intrinsic efficiencies for X- and γ-rays, thus minimizing the potentially confounding count contribution of any such radiations accompanying beta-particle emission [46, 47].

Daghighian et al. [48] have developed and evaluated a plastic scintillator-based positron probe whose design is represented in Fig. 6.30. The basic design of this dual-detector probe includes two scintillator detectors, a central solid-cylinder detector (designated "Detector-1") and a hollow-cylinder detector (designated "Detector-2") in 1-mm-thick stainless steel cladding; the outputs of the two detectors are transmitted by fiber-optic cabling to separate PMTs (PMT 1 and PMT 2, respectively). The Detector-1 counts result from both positrons and the 511-keV annihilation photons associated with positron emission, while the stainless steel cladding of Detector-2 completely attenuates the positrons and allows only the high-energy annihilation photons to enter the detector and generate counts. Because of the different shielding, sensitivities of Detectors 1 and 2 for the 511 keV photons are different. The Detector-1-to-Detector-2 ratio of the measured sensitivities for 511 keV photons is the weighting factor by which the Detector-2 count rate is multiplied and then subtracted from the Detector-1 count rate to yield the Detector-1 positron-only count rate. This probe was evaluated using the phantom setup shown in the figure, with a small ^{18}F-containing capsule simulating a tumor positioned within a uniform ^{18}F-filled cylindrical container simulating underlying normal tissue activity. The probe was then scanned across the phantom, and the Detector-1 and Detector-2 count rates at lateral positions relative to the "tumor" (i.e., capsule) were recorded; the results obtained in terms of the measured count rates and target-to-background ratios (particularly the dramatic improvement from ~2 to ~10 in the target-to-background ratios) clearly demonstrate the feasibility of this dual-detector design and weighted-subtraction algorithm for beta-probes in general and for positron probes in particular.

6.11.1.2 Intraoperative Gamma Cameras

Although the sensitivity and specificity for sentinel lymph node detection using current approaches such as preoperative gamma camera imaging, intraoperative handheld gamma-probes, and the "blue dye" technique are quite high, there remains a need to develop techniques to improving sensitivity and reducing the false-negative rates of sentinel lymph node detection. Intraoperative small FOV gamma camera imaging may provide the improvement required to satisfy such requirements. A gamma camera system having a spatial resolution of 3 mm or better at a distance (depth) of the order of 1 cm would likely visualize such problematic nodes intraoperatively. Such an imaging system would offer other practical advantages over the handheld, non-imaging gamma-probes, as follows:

- The signal is provided in the familiar format of a scintigraphic image rather than a numerical display or a sound with variable frequency tone/pitch.
- The larger FOV of even small dedicated gamma cameras (several cm) than that of gamma-probes (<1 cm) allows more rapid exploration of large areas and/or acquisition of more counts and therefore reduction in statistical uncertainty (noise).
- More straightforward re-examination of the surgical site post-lymph node excision to verify removal of foci of activity.
- Less reliance on potentially obliterated and otherwise ambiguous preoperative skin markings directing where measurements are to be performed intraoperatively [49].

Thus, intraoperative small FOV gamma camera systems merit development and evaluation. A number of small FOV intraoperative gamma camera systems have been developed [43, 50, 51]. The earliest systems were handheld devices

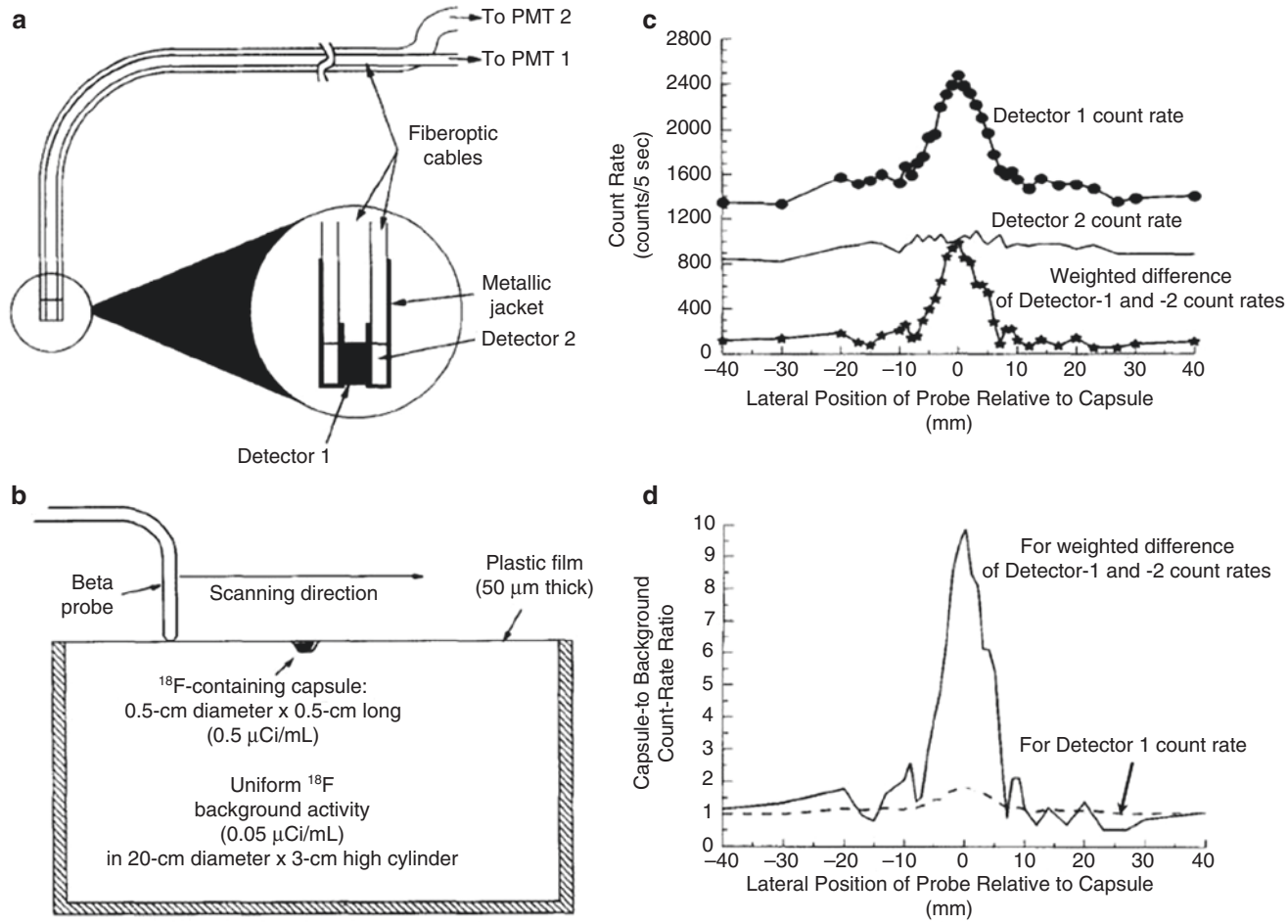

Fig. 6.30 (**a**) Basic design of a dual-detector beta-probe. (**b**) Experimental phantom setup for evaluation of the performance of the probe shown in (**a**). The phantom consisted of a small ^{18}F-containing capsule simulating a tumor and a uniform ^{18}F-filled cylindrical source simulating underlying normal tissue activity. The probe was then scanned across the phantom. Note that the capsule-to-background activity concentration ratio was 10:1. (**c**) The measured Detector-1 and Detector-2 count rates and the calculated weighted difference of the Detector-1 and Detector-2 count rates (see text) as a function of the lateral position of the probe relative to the capsule. (**d**) The capsule-to-background-background count-rate ratios for Detector-1 with and without weighted subtraction (*reproduced from: Daghighian F, Mazziotta JC, Hoffman EJ, Shenderov P, Eshaghian B, Siegel S, et al. Intraoperative beta probe: a device for detecting tissue labeled with positron or electron emitting isotopes during surgery. Med Phys. 1994;21:153–7*)

having FOVs of only 1.5–2.5 cm in diameter and used conventional NaI(Tl) or CsI(Tl) scintillation detectors. Subsequent systems used two-dimensional arrays (mosaics) of scintillation crystals connected to a PSPMT and, more recently, semiconductors such as CdTe or CdZnTe detectors. The main problems with these early units were their very small FOV and the resulting large number of images required to explore the surgical field, associated with the difficulty in holding the device sufficiently still for the duration (up to 1 min) of image acquisition. More recently, larger FOV devices have developed which are attached to an articulating arm for convenient and stable positioning. These systems remain nonetheless fully portable and small enough overall to be accommodated in typical surgical suites.

The *eZSCOPE* (Anzai Medical, Tokyo, Japan) is a handheld CdZnTe-based semiconductor gamma camera. The device is light enough (820 g) to hold for a short time (up to ~1 min). The CdZnTe detector has a 3.2 × 3.2 cm FOV and is 5 mm thick, with an efficiency of 87% and energy resolution of 9% for ^{99m}Tc γ-rays. Its collimators are easily exchanged. The CZT crystal is divided into a 16 × 16 array of 2 × 2 mm pixels, with integral and differential uniformities of 1.6% and 1.3%, respectively, with low-energy high-resolution (LEHR) collimation. The system spatial resolution with the LEHR collimation is 2.3 mm, 8.0 mm, and 15 mm FWHM at source-to-collimator distances of 1 cm, 5 cm, and 10 cm, respectively. As shown in Fig. 6.31, this camera is able to clearly image sentinel lymph nodes as well as lymphatic vessels. However, the small 3.2 × 3.2 cm FOV remains limiting. For example, a single lymph node occupies nearly half of the FOV, and thus searching the surgical field can be time-consuming.

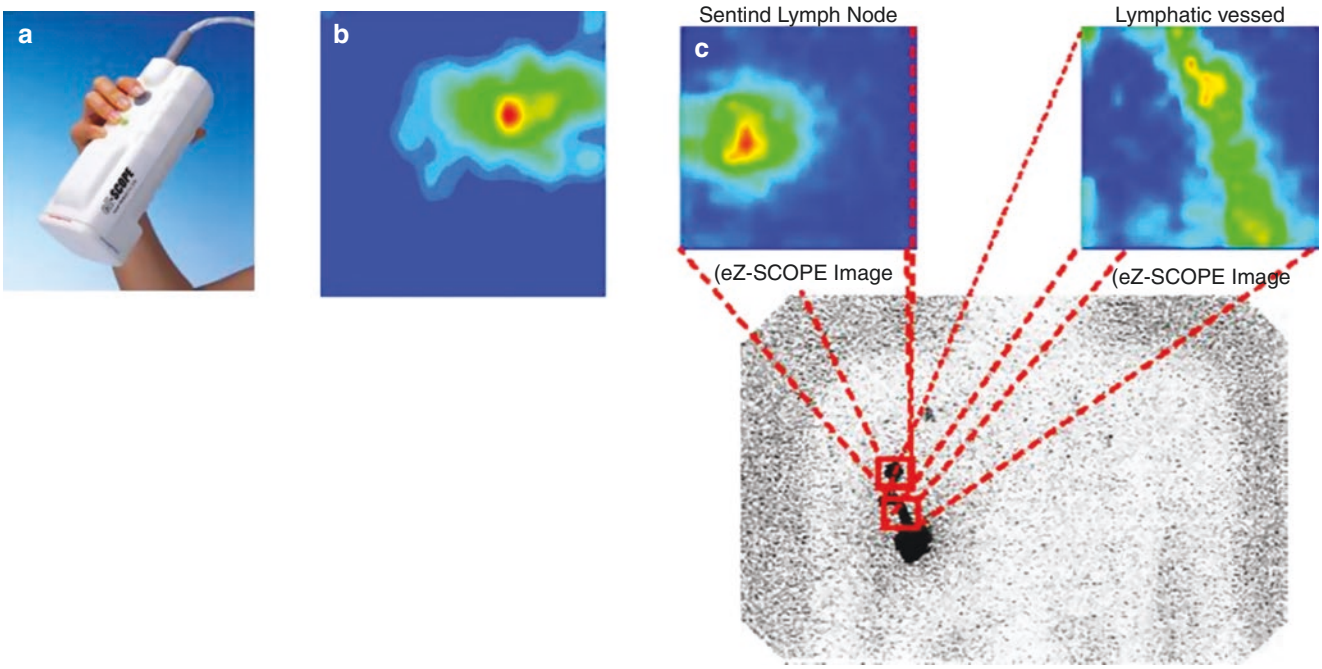

Fig. 6.31 (**a**) Photograph of the eZSCOPE intraoperative gamma camera (Anzai Medical, Tokyo, Japan). (**b**) Sample eZSCOPE image of a lymph node in a patient. (**c**) Sample eZSCOPE images of a lymph node (top left) and lymphatic vessel in a patient (top right) and conventional gamma camera image of the same patient obtained preoperatively (bottom). See text for additional details

General Electric (Haifa, Israel) developed a CdZnTe-based semiconductor gamma camera with a FOVof 4 × 4 cm, larger than that of the eZSCOPE. The 4 × 4 cm pixelated detector consists of a 16 × 16 array of 2.5 × 2.5 mm pixels. Using parallel-hole collimation, the spatial resolution is 5 mm FWHM at a distance of 5 cm, with a sensitivity of 100 cps/MBq. Energy resolution for ^{99m}Tc is 8.0%, somewhat better than the ~10% value typically quoted for conventional gamma cameras. In phantom experiments, this system could clearly resolve ^{99m}Tc-filled spheres 1 cm in diameter in contact with one another at distances of up to 6 cm; a gamma-probe could only distinguish the two sources at a 1 cm depth and only when separated by at least 2 cm. A potential advantage of gamma camera imaging is the ability to resolve sources that may overlap one another in one view by acquiring additional views at different angles, as illustrated by the results of the phantom experiment shown in Fig. 6.32. This feature may be helpful, especially in breast cancer, for localizing a sentinel lymph node at a different depth from the injection site and obscured by the injected activity.

POCI ("Per-operative Compact Imager") is a small FOV gamma camera developed in France. This handheld camera utilizes a CsI(Na) scintillation crystal coupled to a focusing image intensifier tube and position-sensitive diode [52] (Fig. 6.33). Its FOV is 4.0 cm in diameter. With high-resolution parallel-hole collimation, its ^{99m}Tc sensitivity with scatter is 250 cps/MBq at 1 cm and 125 cps/MBq at 5 cm; the corresponding spatial resolution is 3.9 mm, 4.8 mm, and 7.6 mm FWHM at 1 cm, 2 cm, and 5 cm, respectively. Images are acquired in a 50 × 50 pixel matrix. However, energy resolution of the POCI is rather poor (28%), and the wide energy windows thus required result in inclusion of substantial amounts of scatter in the image, a particular disadvantage when a lymph node is close to the injection site. In a preliminary clinical study, lymph nodes in all three patients were identified with the POCI gamma camera, including one in whom two deep nodes were missed with a gamma-probe (most likely due to depth-related loss of sensitivity and proximity of the nodes to the injection site). The total imaging times depended upon the scan area and varied from 15 s to 3 min.

Tsuchimochi and colleagues in Japan [53] developed another semiconductor gamma camera utilizing a CdTe detector. Their choice of CdTe was based on its superior uniformity (4.5% integral uniformity) and energy resolution (7.8%) than CdZnTe. The gamma camera, referred to as the "small semiconductor gamma camera (SSGC)," uses an array of 32 × 32-mm-thick CdTe elements, with a 1.2 × 1.2 mm pixel matrix and a 4.5 × 4.5 cm FOV. The tungsten collimator has 1.2 × 1.2 mm square apertures to match the pixel arrangement. Spatial resolution without scatter is 3.9 mm, 6.3 mm, and 11.2 mm FWHM at 2.5 cm, 5 cm, and 10 cm, respectively. Sensitivity for ^{99m}Tc at the surface without scatter is 300 cps/MBq, comparable to that of the POCI and better than that of a conventional gamma camera with LEHR collimation (~100 cps/MBq). The results of preliminary phantom and clinical imaging studies with the SSGC are encouraging.

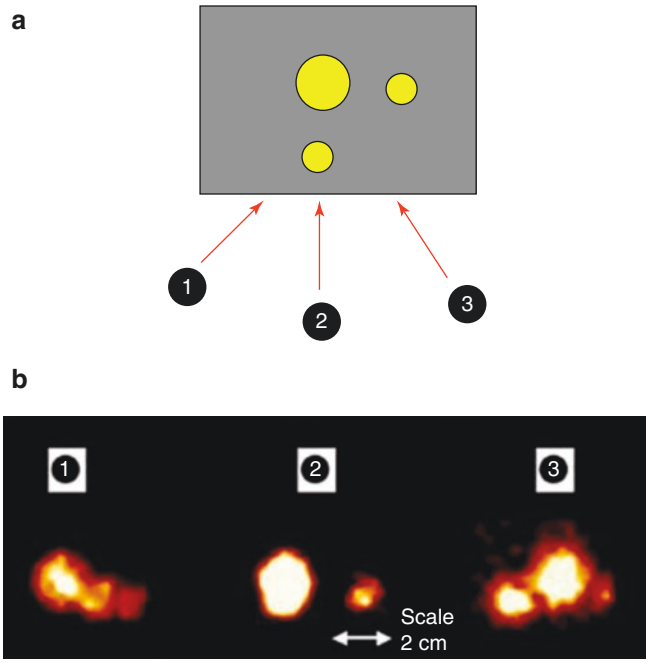

Fig. 6.32 Setup and results of a ^{99m}Tc phantom imaging experiment with the intraoperative gamma camera developed by General Electric (Haifa, Israel). (**a**) Schematic diagram (side view) of phantom, with two 1 cm spheres at depths of 2 and 4 cm and a third sphere, 1.4 cm in diameter, at a depth of 2 cm and directly over the 2 cm sphere at a depth of 4 cm. The two small spheres and the large sphere had activity concentrations of 1 μCi/mL and 2.5 μCi/mL, respectively. (**b**) Images (identified as "1," "2," and "3," respectively) were acquired at angles of −45°, 0°, and +45° relative to an axis perpendicular to the top of the phantom (i.e., an axis in the plane of the diagram). The resulting gamma camera images demonstrate the ability to resolve overlying foci of activity by acquiring views at multiple angles (*reproduced from: Kopelman D, Blevis I, Iosilevsky G, Reznik A, Chaikov A, Weiner N, et al. A newly developed intra-operative gamma camera: performance characteristics in a laboratory phantom study. Eur J Nucl Med Mol Imaging. 2005;32:1217-24*)

Sentinella 102 has been developed by General Equipment for Medical Imaging, South America. It uses a single 4 × 4 cm CsI(Na) scintillation crystal and a PSPMT, images being acquired in a 300 × 300 matrix. Interchangeable pinhole apertures 1.0, 2.5, and 4.0 mm in diameter are available, yielding an effective FOV of 20 × 20 cm at a distance of 18 cm. The detector assembly weighs 1 kg and is mounted on an articulating arm (Fig. 6.34). Sensitivity for ^{99m}Tc ranges from 200 to 2000 cps/μCi at 1 cm and 60–160 cps/μCi at 10 cm, depending on the pinhole aperture used. The FWHM spatial resolution over the detector face is 5.4–8.2 mm, 7.3–11 mm, and 10–18 mm at 3 cm, 5 cm, and 10 cm, respectively, again depending on the pinhole aperture used. Beyond ~3 cm, therefore, spatial resolution is poorer than that of gamma cameras with parallel-hole collimation. However, despite the coarser resolution, the advantage of a pinhole collimation lies in the larger effective FOV at such distances. Such a system can therefore be used at large distances to rapidly survey, with coarser resolution, a large area and then examine suspicious areas at smaller distances and finer resolution [54–56]. In initial clinical studies, acquisition times of 20–60 s per image were required. Because the distortion associated with pinhole collimation varies with position within the FOV (i.e., is worse toward the periphery) as well as distance, the Sentinella 102 camera is equipped with a laser positioning system, two intersecting lines being projected onto the surface of the region being imaged. This allows positioning of suspicious foci of activity at the center of the FOV, where image quality is best. The Sentinella 102 camera is also equipped with a long-lived ^{153}Gd pointer for real-time positioning; the image of the ^{153}Gd pointer source is acquired in a separate energy window from the ^{99m}Tc image and is displayed as a small marker superimposed on the ^{99m}Tc image.

CarolIReS [57] is an intraoperative gamma camera developed by the Institut Pluridisciplinaire Hubert Curien

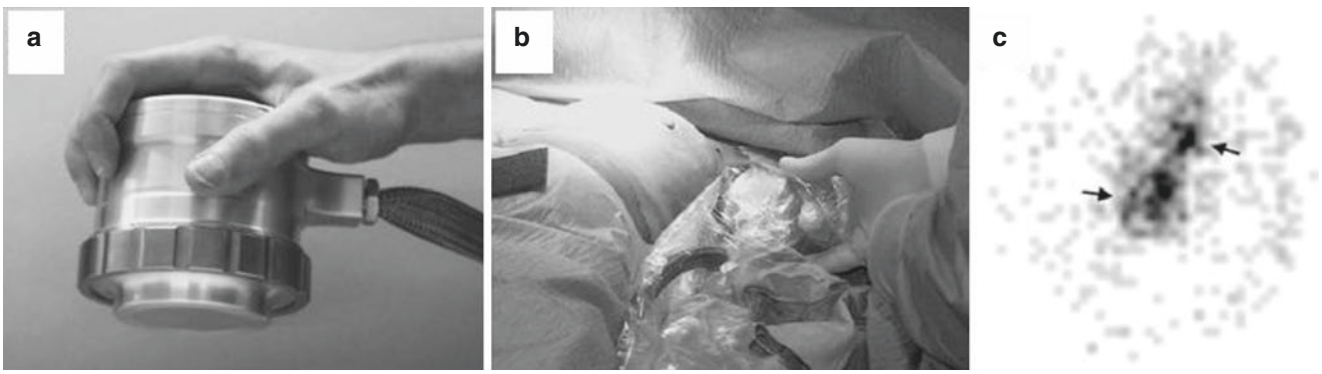

Fig. 6.33 (**a**) Photograph of the POCI (Per-operative Compact Imager) intraoperative gamma camera. (**b**) Intraoperative lymphoscintigraphy, with the POCI in position for imaging of the patient's left axilla. (**c**) POCI image (10-s acquisition time), showing two foci of activity corresponding to two neighboring lymph nodes (*reproduced from: Pitre S, Menard L, Ricard M, Solal M, Garbay JR, Charon Y. A hand-held imaging probe for radio-guided surgery: physical performance and preliminary clinical experience. Eur J Nucl Med Mol Imaging. 2003;30:339–43*)

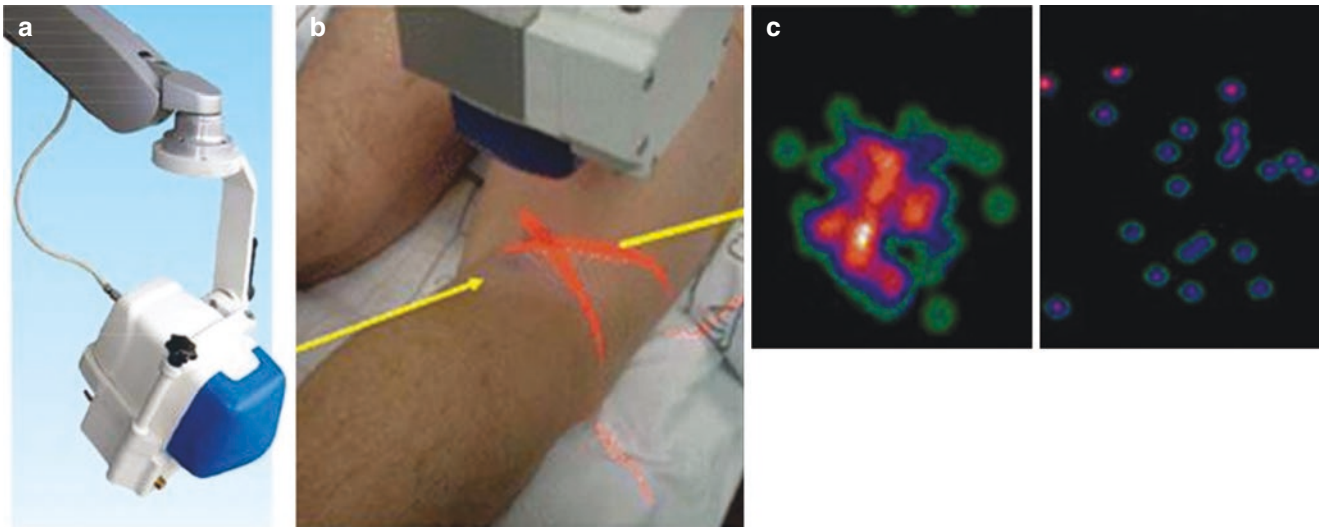

Fig. 6.34 (**a**) Photograph of the Sentinella 102 small FOV gamma camera (General Equipment for Medical Imaging, South America). The detector assembly is shown mounted on the system's articulating arm. (**b**) Illustration of the device's laser positioning system, with two intersecting red lines projected onto posterior surface of the patient's right knee joint. This patient had malignant melanoma of the right heel, and lymphoscintigraphy was performed to identify the popliteal sentinel lymph node. (**c**) Posterior gamma camera images of the patient's right knee joint before (left) and after (right) surgical excision of the popliteal node. The pre-excision image (left) clearly shows the node centered in the field of view, and the post-excision image (right) is notably absent of any such focus of activity, demonstrating complete removal of the node

(Strasbourg, France). This device has a relatively large-area 50 × 50 mm cerium-doped gadolinium ortho-oxysilicate (GSO(Ce)) scintillation crystal and is equipped with a parallel-hole collimator with 2-mm-wide apertures. Its ^{99m}Tc spatial resolution is 10 mm FWHM at 5 cm, sensitivity is 130 cpm/kBq, and energy resolution is 45%. A prototype version of this device with a larger 100 × 100 mm FOV has been developed as well. In a preliminary clinical study with the CarolIReS camera, Mathelin et al. [58] compared the depth of lymph nodes estimated by imaging to their actual depth measured at surgery and found a generally good correlation except in instances where only a portion of the sentinel lymph node was in the camera's FOV. For 7/11 lymph nodes whose depth could be estimated, the image-derived depth was correct.

Overall, small FOV gamma cameras have demonstrated detection rates for sentinel lymph nodes equal to or better than those of non-imaging gamma-probes, despite the fact that their sensitivities (e.g., expressed in cps/MBq) are typically about tenfold lower than those of the handheld on-imaging gamma-probes. The ability of such devices to image a surgical field intraoperatively and thus verify complete excision of lesions is a potentially useful enhancement of the radioguided surgery techniques employed in cancer patients. The acquisition times per image are typically well under 1 min, so the overall duration of the surgical procedure is not significantly prolonged. Furthermore, despite having lower sensitivity than parallel-hole collimation, the use of pinhole collimation permits initial imaging at longer distance to visualize a larger anatomic area of interest, followed by imaging at shorter distance to pinpoint and otherwise characterize suspicious foci of activity. Finally, the scintigraphic image format is familiar to surgeons, thus facilitating clinical acceptance and integration of intraoperative imaging.

Intraoperative PET scanners. Prescient Imaging LLC is currently developing a portable compact whole-body PET scanner adaptable to intraoperative imaging [59]. It incorporates a 360° detector system with an axial FOV of 22 cm. The detectors are assembled into three sets, one planar and the other two circular arcs of 90° each connected with a hinge. One of the arcs is fixed, while the other can be rotated about the hinge and thereby opened and closed. The planar detector is fixed horizontally, such that it can fit under a patient table. By placing the moveable arc in the closed position, a 360° of detector coverage about the patient is achieved. Attenuation correction can be performed using a rotating rod transmission source.

Key Learning Points

- Handheld gamma-probes for radioguided surgery have been developed for a wide variety of applications.
- The detector component of handheld gamma-probes for radioguided surgery can be either a scintillation crystal or a solid-state detector.
- Beta-probes designed for special applications based on the use of PET radiopharmaceuticals have also been developed.
- Small-field-of-view gamma cameras for use during surgery are also commercially available.

Glossary

APD	Avalanche photodiode
BGO	Bismuth germanate
CsI(Na)	Sodium-activated cesium iodide
CsI(Tl)	Thallium-activated cesium iodide
FOV	Field of view
FWHM	Full width at half maximum
G-APD	Geiger-mode avalanche photodiode
GM	Geiger-Müller
HEAP	High-energy all-purpose
HEGP	High-energy general-purpose
IP	Imaging probe
LEAP	Low-energy all-purpose
LEGP	Low-energy general-purpose
LEHR	Low-energy high-resolution
LYSO(Ce)	Cerium-doped lutetium yttrium orthosilicate
MEAP	Medium-energy all-purpose
MEGP	Medium-energy general-purpose
NaI(Tl)	Thallium-activated sodium iodide
PET	Positron emission tomography
PMT	Photomultiplier tube
PSM	Prone scintimammography
PSPMT	Position-sensitive PMT
RIGS	Radioimmunoguided surgery
SM	Scintimammography
SN	Sentinel node
SNR	Signal-to-noise ratio
SPECT	Single-photon emission computed tomography
SPECT/CT	Single-photon emission computed tomography/computed tomography
SPEM	Single-photon emission mammography
YAlO3(Ce)	Cerium-activated yttrium aluminum perovskite
YAP(Ce)	Cerium-activated yttrium aluminum perovskite

References

1. Anger HO. Scintillation camera. Rev Sci Instrum. 1958;29:27–33.
2. Pani R. Nuclear medicine: special applications in functional imaging. In: Del Guerra A, editor. Ionizing radiation detectors for medical imaging. Singapore: World Scientific Pub. Co. Inc; 2004. p. 359–83.. ISBN: 978-9812386748.
3. Zanzonico P, Heller S. Physics, instrumentation, and radiation protection. In: Biersack H-J, Freeman LM, editors. Clinical nuclear medicine. Heidelberg: Springer; 2007. p. 1–33.
4. Zanzonico P. Principles of nuclear medicine imaging: planar, SPECT, PET, multi-modality, and autoradiography systems. Radiat Res. 2012;177:349–64.
5. Zanzonico P. Radionuclide imaging. In: Cherry S, Badawy R, Qi J, editors. Essentials of in vivo biomedical imaging. Boca Raton, FL: CRC Press; 2015. p. 1765–224.
6. Slomka PJ, Berman DS, Germano G. New cardiac cameras: single-photon emission CT and PET. Semin Nucl Med. 2014;44:232–51.
7. Slomka PJ, Pan T, Berman DS, Germano C. Advances in SPECT and PET hardware. Prog Cardiovasc Dis. 2015;57:566–78.
8. Fong Y, Giulianotti PC, Lewis J, Koerkamp BG, Reiner T, editors. Imaging and visualization in the modern operating room. A comprehensive guide for physicians. Berlin: Springer; 2015.. ISBN: 978-1-4939-2325-0.
9. Hofstadter R. Alkali halide scintillation counters. Phys Rev. 1948;74:100–1.
10. Hofstadter R. Scintillation counters; Research reviews. Arlington, VA: Office of Naval Research.. 4 (September, 1949):4-8. Also in Nucleonics. 1950;6:70.
11. Weber MJ, Monchamp RR. Luminescence of Bi4 Ge3 O12: spectral and decay properties. J Appl Phys. 1973;44:5495–9.
12. Baryshevsky VG, Korzhik MV, Moroz VI, Pavlenko VB, Fyodorov AA, Smirnova SA, et al. YAlO3:Ce fast-acting scintillators for detection of ionizing radiation. Nucl Instr Meth B. 1991;58:291–3.
13. Morinaga H, Gugelot PC. Gamma rays following (α,xn) reactions. Nucl Physics. 1963;46:210–24.
14. Anger HO. A multiple scintillation counter in vivo scanner. Am J Roentgenol Ther Nucl Med. 1953;70:605–12.
15. Casey ME, Nutt R. A multicrystal two dimensional BGO detector system for positron emission tomography. IEEE Trans Nucl Sci. 1986;33:460–3.
16. Del Guerra A, Belcari N, Bisogni M. Positron emission tomography: its 65 years. Rivista del Nuovo Cimento. 2016;39-4:155–223.
17. Blazek KJ, Vrzala VP. Composite detector of bismuth germanate mono-crystals. Czechoslovakian Patent no. 256143. Registered 15-04-1986.
18. Pani R, Pellegrini R, Soluri A, De Vincentis G, Scafè R, Pergola A. Single photon emission imaging by position sensitive PMT. Nucl Instr Meth A. 1998;409:524–8.
19. Shao Y, Silverman RW, Cherry SR. Evaluation of Hamamatsu R5900 series PMTs for readout of high-resolution scintillator arrays. Nucl Instr Meth A. 2000;454:379–88.
20. Pani R, Soluri A, Scafè R, Pergola A, Pellegrini R, De Vincentis G, et al. Multi-PSPMT scintillating camera. IEEE Trans Nucl Sci. 1999;46:702–8.
21. Kyushima H, Shimoi H, Atsumi A, Ito M, Oba K, Yoshizawa Y. The development of flat panel PMT. IEEE Nucl Sci Symp Conf Rec. 2000;1:7/3–7. https://doi.org/10.1109/NSSMIC.2000.949246.
22. Scafè R, Pellegrini R, Cinti MN, Puccini M, Pani R. A novel scintillation imager with charge-spread discrimination.Analytical models suitable for crystal-arrays. Nucl Instr Meth A. 2016;833:110–21.
23. Renker D. Geiger-mode avalanche photodiodes, history, properties and problems. Nucl Instr Meth A. 2006;567:48–56. https://doi.org/10.1016/j.nima.2006.05.060.
24. Khalkali I, Mena I, Jouanna E, Diggles L, Venegas R, Block J, et al. Prone scintimammography in patients with suspicion of carcinoma of the breast. J Am Coll Surg. 1994;178:491–7.
25. Scopinaro F, Schillaci O, Scarpini M, Mingazzini L, Di Macio L, Banci M, et al. Technetium-99m sestamibi: an indicator of breast cancer invasiveness. Eur J Nucl Med. 1994;21:984–7.
26. Garibaldi F, Cisbani E, Cusanno F, Iommi R, Urciuoli GM, Pani R, et al. Optimization of compact gamma cameras for breast imaging. Nucl Instr Meth A. 2003;471:222–8.
27. De Vincentis G, Scopinaro F, Pani R, Pellegrini R, Soluri A, Ierardi M, Ballesio L, Weinberg IN, Pergola A. 99mTc MIBI scintimammography with a high resolution single tube gamma camera: preliminary study. Anticancer Res. 1997;17(3B):1627–30.
28. De Vincentis G, Gianni W, Pani R, Cacciafesta M, Pellegrini R, Soluri A, et al. Role of ^{99m}Tc-Sestamibi scintimammography by SPEM camera in the management of breast cancer in the elderly. Breast Cancer Res Treat. 1998;48:159–63.
29. Pani R, Pellegrini R, De Vincentis G, Cinti MN, Weinberg IN, Soluri A, et al. Factors affecting cancer detectability in Tc-99m MIBI scintimammography. Nucl Instr Meth A. 2003;497:90–7.

30. Gambaccini M, Fantini A, Bollini D, Castelli E, Del Guerra A, Di Domenico G, et al. Development of a quasi-monochromatic CT system for breast cancer study with combined emission-transmission tomography. IEEE Trans Nucl Sci. 2001;48:703–6.
31. Travin MI. Cardiac cameras. Semin Nucl Med. 2011;41:182–201.
32. Sweet WH. The uses of nuclear disintegration in the diagnosis and treatment of brain tumors. N Engl J Med. 1951;245:875–8.
33. Harris CC, Bigelow RR, Francis JE, Kelley GG, Bell PR. A CsI(Tl)-crystal surgical scintillation probe. Nucleonics. 1956;14:102–8.
34. Hoffman EJ, Tornai MP, Janecek M, Patt BE, Iwanczyk JS. lntraoperative probes and imaging probes. Eur J Nucl Med. 1999;26:1913–35.
35. Knoll GF, Lieberman LM, Nishiyama H, Beierwaltes WH. A gamma ray probe for the detection of ocular melanomas. IEEE Trans Nucl Sci. 1972;19:76–80.
36. Pircher FJ, Anderson B, Cavanaugh PJ, Sharp KW. Experiences with a solid state detector for surface counting of phosphorus-32. J Nucl Med. 1967;8:444–50.
37. Lauber A. Development of miniaturized solid state detectors for the measurement of beta and gamma radiation in superficial and deep parts of living tissue. Nucl Instr Meth. 1972;101:545–50.
38. Soluri A, Scafè R, Scopinaro F, Bruschi R, Casasanta V, Latini R, et al. The imaging probe: miniaturized gamma camera. In: Limouris GS, Biersack HJ, Kouros KC, editors. Radionuclides for lymph node mapping – current status and future aspects. Athens: Mediterra Publishers; 1999. p. 67–72.. ISBN 960-86437-0-8.
39. Pani R, Soluri A, Scafè R, Pellegrini R, Tatì A, Scopinaro F, et al. A compact gamma ray imager for oncology. Nucl Instr Meth A. 2002;477:509–13.
40. Pani R, de Notaristefani F, Blazek K, Maly P, Pellegrini R, Pergola A, et al. Multi-crystal YAP:Ce detector system for position sensitive measurements. Nucl Instr Meth A. 1994;348:551–8.
41. Truman A, Bird AJ, Ramsden D, He Z. eCsI(Tl) arrays with position-sensitive PMT readout. Nucl Instr Meth A. 1994;353:375–8.
42. Woolfenden JM, Barber HB. Intraoperative probes. In: Wagner Jr HN, Szabo Z, editors. Principles of nuclear medicine. 2nd ed. Philadelphia, PA: WB Saunders; 1995. p. 292–7.
43. Heller S, Zanzonico P. Nuclear probes and intraoperative gamma cameras. Semin Nucl Med. 2011;41:166–81.
44. Essner R, Daghighian F, Giuliano AE. Advances in FDG PET probes in surgical oncology. Cancer J. 2002;8:100–8.
45. Strong VE, Galanis CJ, Riedl CC, Longo VA, Daghighian F, Humm JL, et al. Portable PET probes are a novel tool for intraoperative localization of tumor deposits. Ann Surg Innov Res. 2009;3:2.
46. Schneebaum S, Essner R, Even-Sapir E. Positron-sensitive probes. In: Mariani G, Giuliano AE, Strauss HW, editors. Radioguided surgery – a comprehensive team approach. New York, NY: Springer; 2008. p. 23–8.
47. Raylman RR. Performance of a dual, solid-state intraoperative probe system with ^{18}F, ^{99m}Tc, and ^{111}In. J Nucl Med. 2001;42:352–60.
48. Daghighian F, Mazziotta JC, Hoffman EJ, et al. Intraoperative beta probe: a device for detecting tissue labeled with positron or electron emitting isotopes during surgery. Med Phys. 1994;21:153–7.
49. Britten AJ. A method to evaluate intra-operative gamma probes for sentinel lymph node localisation. Eur J Nucl Med. 1999;26:76–83.
50. Hoffman EJ, Tornai MP, Levin CS. Gamma and beta intra-operative imaging probes. Nucl Instr Methods Phys Res. 1997;392:324–32.
51. Scopinaro F, Soluri A. Gamma ray imaging probes for radioguided surgery and site-directed biopsy. In: Mariani G, Giuliano AE, Strauss HW, editors. Radioguided surgery. New York, NY: Springer; 2008. p. 29–36.
52. Pitre S, Menard L, Ricard M, et al. A hand-held imaging probe for radio-guided surgery: physical performance and preliminary clinical experience. Eur J Nucl Med Mol Imaging. 2003;30:339–43.
53. Tsuchimochi M, Hayama K, Oda T, et al. Evaluation of the efficacy of a small CdTe gamma-camera for sentinel lymph node biopsy. J Nucl Med. 2008;49:956–62.
54. Sanchez F, Benlloch JM, Escat B, et al. Design and tests of a portable mini gamma camera. Med Phys. 2004;31:1384–97.
55. Sanchez F Fernandez MM, Gimenez M, et al. Performance tests of two portable mini gamma cameras for medical applications. Med Phys. 2006;33:4210–20.
56. Ortega J, Ferrer-Rebolleda J, Cassinello N, et al. Potential role of a new hand-held miniature gamma camera in performing minimally invasive parathyroidectomy. Eur J Nucl Med Mol Imaging. 2007;34:165–9.
57. Mathelin C, Salvador S, Bekaert V, et al. A new intraoperative gamma camera for the sentinel lymph node procedure in breast cancer. Anticancer Res. 2008;28:2859–64.
58. Mathelin C, Salvador S, Huss D, et al. Precise localization of sentinel lymph nodes and estimation of their depth using a prototype intraoperative mini gamma-camera in patients with breast cancer. J Nucl Med. 2007;48:623–9.
59. Daghighian F, Fong Y. Detectors for intraoperative molecular imaging: from probes to scanners. In: Fong Y, Giulianotti PC, Lewis J, Koerkamp BG, Reiner T, editors. Imaging and visualization in the modern operating room: a comprehensive guide for physicians. New York, NY: Springer; 2015. p. 55–67.

Further Reading

Books

Cherry SR, Sorenson JA, Phelps ME. Physics in nuclear medicine. 4th ed. Philadelphia, PA: Elsevier Saunders; 2012. ISBN: 978-1-4160-5198-5.

DeWerd L, Kissick M, editors. The phantoms of medical and health physics. Devices for research and development. New York, NY: Springer; 2014. ISBN: 978-1-4614-8303-8.

Flower MA, editor. Webb's physics of medical imaging. 2nd ed. Boca Raton, FL: CRC Press, Taylor & Francis Group; 2012. ISBN: 978-1-4665-6895-2.

Giussani A, Hoeschen C, editors. Imaging in nuclear medicine. New York, NY: Springer; 2013. ISBN: 978-3-642-31414-8.

Godfrey DJ, Das SK, Wolbarst AB, editors. Advances in medical physics. 5th ed. Madison, WI: Medical physics publishing; 2014. ISBN: 978-1-930524-63-7.

IAEA. Human health series no. 29. Guided intraoperative scintigraphic tumour targeting (GOSTT); implementing advanced hybrid molecular imaging and non-imaging probes for advanced cancer management. Wien: International Atomic Energy Agency; 2014. ISBN:978-92-0-102214-1.

Iwanczyk JS, editor. Radiation detectors for medical imaging. Boca Raton, FL; London; New York, NY: CRC Press, Taylor & Francis Group; 2015. ISBN: 978-1-4987-0435-9.

Khalkhali I. In: Maublant JC, Goldsmith SJ, editors. Nuclear oncology. Diagnosis and therapy. Philadelphia, PA: Lippincott Williams & Wilkins; 2000. ISBN 0-7817-1990-9.

Knoll GF. Radiation detection and measurement. 3rd ed. New York, NY; Chichester; Weinheim; Brisbane, QLD; Toronto, ON; Singapore: John Wiley & Sons, Inc.; 1999. ISBN 0-471-07338-5.

Mariani G, Giuliano AE, Strauss HW, editors. Radioguided surgery - a comprehensive team approach. New York, NY: Springer; 2008. 978-0-387-33684-8.

Martin C, Sutton D, editors. Practical radiation protection in healthcare. 2nd ed. Oxford: Oxford University Press; 2015. ISBN: 9780199655212.

Perkins A, Lees JE. Gamma cameras for interventional and intraoperative imaging. Boca Raton, FL; London; New York, NY: CRC Press, Taylor & Francis Group; 2016. ISBN 9781498729284.

Phelps ME, editor. PET: physics, instrumentation and scanners. New York, NY: Springer; 2006. ISBN: 978-0-387-32302-2.

Zaidi H, editor. Molecular imaging of small animals. Instrumentation and applications. New York, NY: Springer; 2014. ISBN: 978-1-4939-0893-6.

Review Articles/Chapters

Bricou A, Duval M-A, Charon Y, Barranger E. Mobile gamma cameras in breast cancer care – a review. Eur J Surg Oncol. 2013;39:409–16.

Fontein DBY, van de Water W, Sven J, Mieog D, Liefers G-J, van de Velde CJH. Timing of the sentinel lymph node biopsy in breast cancer patients receiving neoadjuvant therapy – recommendations for clinical guidance. Eur J Surg Oncol. 2013;39:417–24.

Gullberg GT, Reutter BW, Sitek A, Maltz JS, Budinger TF. Topical review – dynamic single photon emission computed tomography - basic principles and cardiac applications. Phys Med Biol. 2010;55:R111–91.

Peterson TE, Furenlid LR. Topical review – SPECT detectors: the Anger Camera and beyond. Phys Med Biol. 2011;56:R145–82.

Povoski SP, Neff RL, Mojzisik CM, O'Malley DM, Hinkle GH, Hall NC, et al. A comprehensive overview of radioguided surgery using gamma detection probe technology. World J Surg Oncol. 2009;7:11. https://doi.org/10.1186/1477-7819-7-11.

Tsuchimochi M, Hayama K. Intraoperative gamma cameras for radioguided surgery: technical characteristics, performance parameters, and clinical applications – review paper. Phys Med. 2013;29:126–38.

Van Audenhaege K, Van Holen R, Vandenberghe S, Vanhove C, Metzler SD, Moore SC. Review of SPECT collimator selection, optimization, and fabrication for clinical and preclinical imaging. Med Phys. 2015;42:4796–813.

Zanzonico P. Instrumentation for positron emission imaging. In: Strauss HW, Mariani G, Volterrani D, Larson SM, editors. Nuclear oncology – from pathophysiology to clinical applications. New York, NY: Springer; 2017. p. 217–50.

Zanzonico P. Instrumentation for single-photon emission imaging. In: Strauss HW, Mariani G, Volterrani D, Larson SM, editors. Nuclear oncology – from pathophysiology to clinical applications. New York, NY: Springer; 2017. p. 251–74.

Zanzonico P. Instrumentation for intraoperative detection. In: Strauss HW, Mariani G, Volterrani D, Larson SM, editors. Nuclear oncology – from pathophysiology to clinical applications. New York, NY: Springer; 2017. p. 275–304.